JOURNAL OF GEOPHYSICAL RESEARCH, VOL. 112, B06419, doi:10.1029/2006JB004860, 2007

Magma intrusion and deformation predictions: Sensitivities to the Mogi assumptions

Timothy Masterlark[1]

Received 16 November 2006; revised 29 January 2007; accepted 15 February 2007; published 26 June 2007.

[1] Mogi's (1958) magma intrusion model is widely used to predict observed deformation of active volcanoes. The model simulates a small spherical expansion source (SES) embedded in a homogeneous, isotropic, Poisson-solid half-space (HIPSHS). This study computes surface displacement due to SESs at depth using a combination of analytical and finite element models (FEMs), for which the HIPSHS assumptions are not required. Interferometric synthetic aperture radar (InSAR) data suggest that Okmok volcano, Alaska, subsided more than a meter owing to lava extrusion during its 1997 eruption. Inverse methods, which use an HIPSHS model, precisely locate an SES at a depth of 3100 m beneath the center of the caldera. A series of alternative model configurations relax the combined suite of HIPSHS assumptions and sequentially isolate the effects of each assumption. Forward modeling predictions are relatively insensitive to topographic effects and layered elastic properties, somewhat sensitive to anisotropic elastic properties and Poisson's ratio, and very sensitive to the presence of weak materials within a caldera. Inverse methods, combined with analytical and FEM-generated impulse response functions, isolate the influence of each HIPSHS assumption on SES depth and pressure estimations. Results are particularly sensitive to a model configuration simulating a weak caldera, for which the estimated SES depth (4500 m) is significantly deeper than the estimate for the HIPSHS model. For deformation data having high signal-to-noise ratios, such as the co-eruption InSAR data for Okmok volcano, both forward and inverse deformation prediction errors attributed to the Mogi (1958) assumptions can greatly exceed observation uncertainties.

Citation: Masterlark, T. (2007), Magma intrusion and deformation predictions: Sensitivities to the Mogi assumptions, *J. Geophys. Res.*, *112*, B06419, doi:10.1029/2006JB004860.

1. Introduction

[2] Understanding the behavior of restless volcanoes depends on both the availability and interpretation of physical measurements. Interferometric synthetic aperture radar (InSAR) data revolutionized our view of active volcano deformation by providing the means to monitor the deformation of known active volcanoes, as well as prospect for deformation signals of awakening dormant volcanoes from a remote sensing platform. Analyses of InSAR data illuminated the interior processes for several Aleutian volcanoes that were either poorly instrumented or entirely uninstrumented owing to their remote locations [*Kwoun et al.*, 2006; *Lu and Freymueller*, 1998; *Lu et al.*, 1998, 2000a, 2000b, 2000c, 2002a, 2002b, 2002c, 2003a, 2003b, 2005a, 2005b; *Mann et al.*, 2002; *Masterlark and Lu*, 2004; *Masterlark et al.*, 2006; *Moran et al.*, 2006; *Price*, 2004]. A variety of source mechanisms have been proposed to account for the observed deformation of volcanoes, such as magma intrusion, slip along faults, pore pressure variations in transient hydrothermal systems, thermoelastic heating or cooling of bodies near the surface and at depth, and poroelastic and viscoelastic relaxation due to surface loading. In terms of predicting eruption activity, some of these deformation sources may be cause for concern, while others may not. For example, deformation caused by restless magma can be a harbinger for an impending eruption [*Sturkell et al.*, 2006; *Vogfjörd et al.*, 2005]. Conversely, thermoelastic deformation caused by a cooling volcanic body can be innocuous [*Masterlark et al.*, 2006].

[3] It is difficult to directly observe the processes at depth that cause the observed deformation at the Earth's surface. Models provide the linkage between observed deformation and the inaccessible deformation source. The analytical solutions of *Mogi* [1958] produce readily predictable deformation patterns due to a spherical expansion source; embedded in a homogeneous, isotropic, Poisson-solid half-space (HIPSHS) problem domain (Figure 1). Others developed analytical solutions or correction schemes to simulate nonspherical expansion source geometries embedded in HIPSHS problem domains [*Beauducel et al.*, 2004; *Bonaccorso and Davis*, 1999; *Fialko et al.*, 2001; *Gottsmann et al.*, 2006b; *Masterlark and Lu*, 2004; *Okada*, 1992; *Yang*

---

[1] Department of Geological Sciences, University of Alabama, Tuscaloosa, Alabama, USA.

0148-0227/07/2006JB004860$09.00

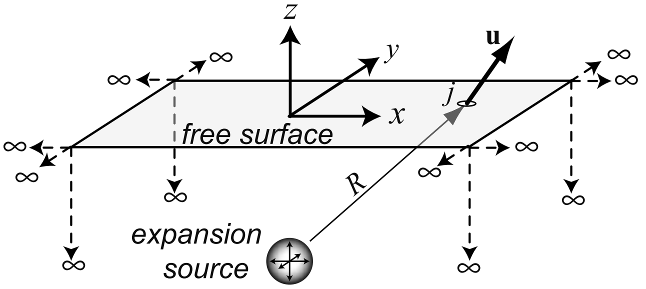

Figure 1. Spherical expansion source embedded in a homogeneous, isotropic, Poisson-solid half-space. The displacement (u) is inversely proportional to the cube of the Euclidean distance (R) separating the center of the spherical expansion source and a point on the free surface (j). This model, often invoked to simulate deformation due to magma intrusion at depth, is subject to the following assumptions and limitations: (1) lateral and depth boundaries extending to infinity, (2) no topography, (3) no layering or spatial variations in the crust, (4) no preferred orientations or fabrics; all cracks or faults must have a random distribution that can be represented as a homogeneous and isotropic elastic continuum, and (5) Poisson's ratio = 0.25.

et al., 1988; *Yun et al.*, 2006]. Alternatively, formulations for nonhomogeneous problem domains include spherical expansion sources either embedded in horizontally layered elastic half-spaces [e.g., *Fernández et al.*, 1997; *Rundle*, 1980] or surrounded by thin viscoelastic shells that are embedded in an elastic full-space [*Dragoni and Magnanensi*, 1989]. The computational simplicity of the above deformation models, particularly that of *Mogi* [1958], is amenable to quantitative optimizations of both linear (expansion source strength) and nonlinear (geometric) parameters. Substantial effort has gone into the development of inverse prediction schemes that strive to accurately characterize the location, geometry, and strength of deformation sources, on the basis of observed deformation data [e.g., *Cervelli et al.*, 2001]. However, relatively little attention is given to the implications of the particular deformation model at the core of an optimization scheme.

[4] The use of finite element models (FEMs) to study volcano deformation is not new. More than three decades ago, *Dieterich and Decker* [1975] assessed prediction sensitivities to various spherical and nonspherical deformation source geometries, embedded in HIPSHS problem domains. A conclusion of *Dieterich and Decker* [1975] is that various source geometries can produce similar vertical deformation patterns, but the horizontal components of deformation are much more sensitive to the source geometry. More recent FEM-based studies of volcano deformation also investigated sensitivities to the geometry of the expansion source [*Yang et al.*, 1988] and *Newman et al.* [2001, 2006] used FEMs to investigate deformation caused by spherical and prolate spheroid expansion sources, having viscoelastic shells, embedded in an HIPSHS. Others used FEMs to account for heterogeneous caldera configurations and structural discontinuities in stress [*Troise et al.*, 2003] and deformation predictions [*Bonaccorso et al.*, 2005; *De Natale and Pingue*, 1996; *De Natale et al.*, 1997; *Orsi et al.*, 1999; *Poland et al.*, 2006; *Trasatti et al.*, 2003, 2005]. The fixed geometric configurations of the FEMs are often based on the results of nonlinear optimization schemes for HIPSHS models [*Bonaccorso et al.*, 2005; *Gottsmann et al.*, 2006a; *Trasatti et al.*, 2005]. I address the implications for each of the HIPSHS assumptions inherent to *Mogi*'s [1958] spherical expansion source model (Figure 1) that is widely used to interpret volcano deformation data, using both forward and inverse models of InSAR data that map deformation of the 1997 eruption of Okmok volcano, Alaska, as an example.

1.1. Site

[5] Umnak Island, located in the central part of the Aleutian arc, consists of two lobes that are aligned northeast-southwest and connected by an isthmus. Vsevidof volcano occupies the southwest portion of the southwest lobe and Okmok volcano occupies the entire northeast lobe of Umnak Island (Figure 2). *Miller et al.* [1998b] describes

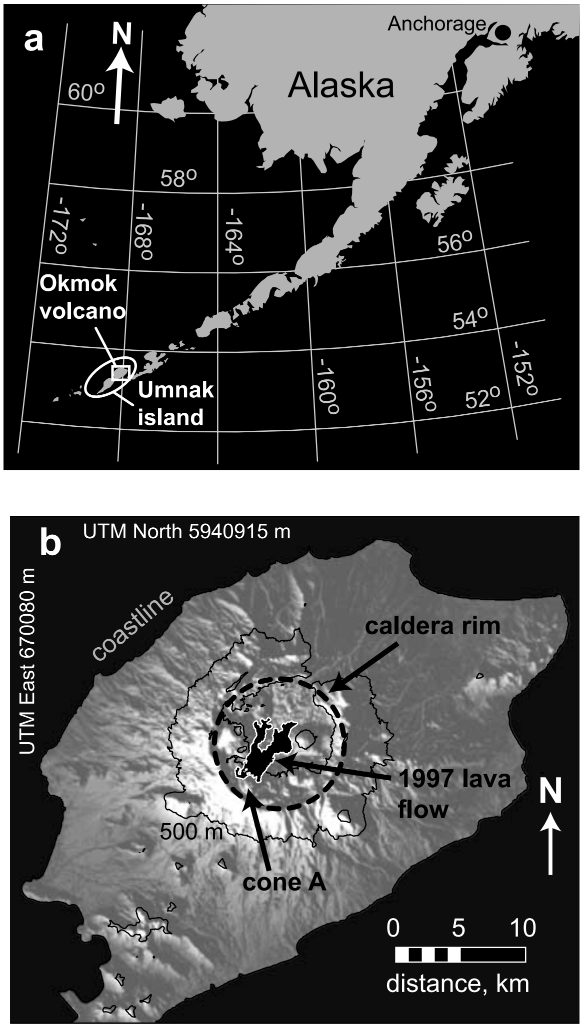

Figure 2. (a) Central Aleutian arc, Alaska. Okmok volcano occupies the northeastern part of Umnak Island of the central Aleutian arc, Alaska. (b) Okmok volcano. The shaded relief image of a digital elevation model reveals the radial symmetry of Okmok's caldera. The maximum elevation is about 1200 m, and the caldera floor has an average elevation of about 450 m.

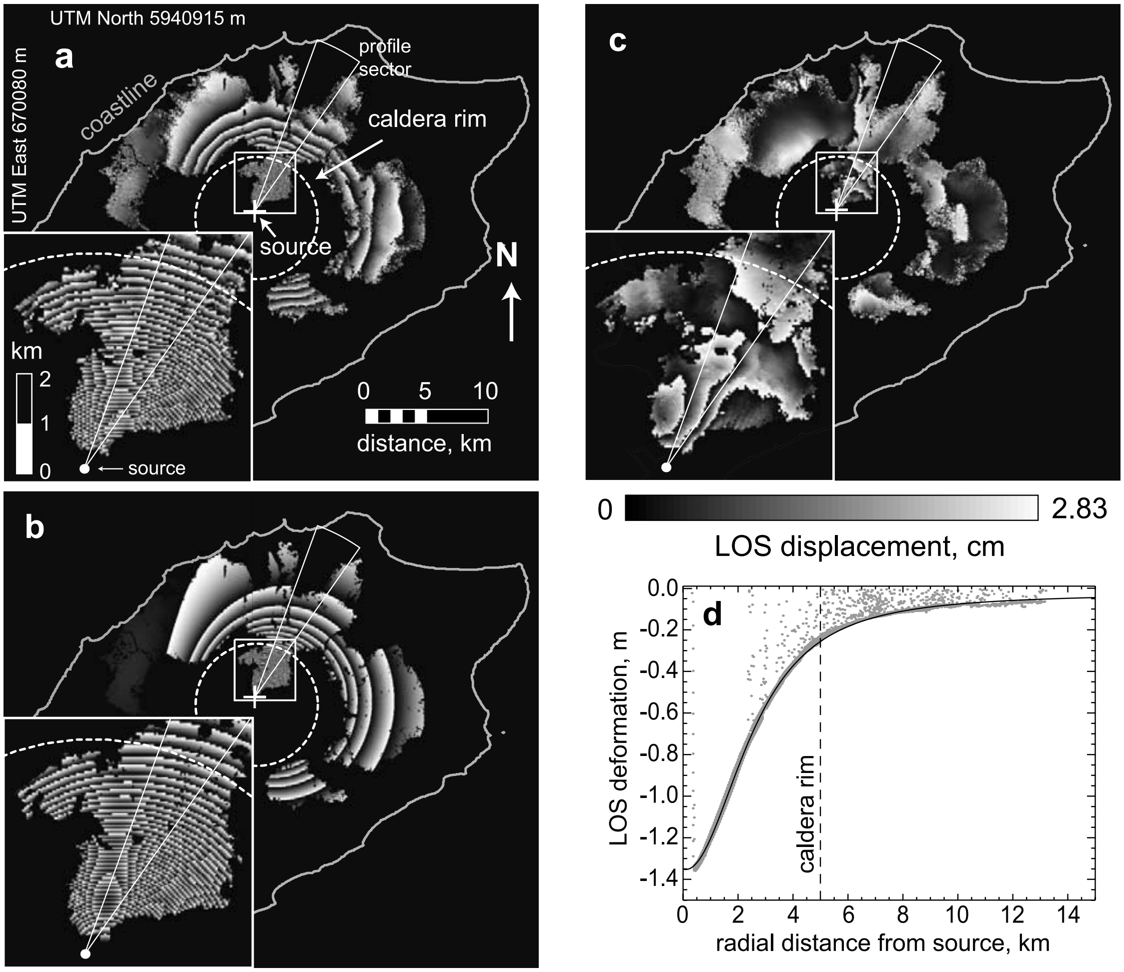

Figure 3. Interferometric synthetic aperture radar (InSAR) data and best fit homogeneous, isotropic, Poisson-solid half-space (HIPSHS) model predictions. Each fringe, black-gray-white, represents 2.83 cm of deformation parallel to the line of sight (LOS) vector and toward the satellite. (a) InSAR data. The InSAR data, spanning the interval 9 October 1995 through 9 September 1997, suggest volcano-wide deformation and almost 1.5 m of subsidence in the caldera. The boundary of the caldera is outlined with the white dashed circle. The radial symmetry and shape of the deformation pattern suggest that a spherical expansion source located beneath the center of the caldera can account for the observed deformation. The assumed horizontal components of the source location are (ξ_x, ξ_y) = (20,700 m, −16,900 m) with respect to the top left corner of the image. The inset shows an expanded view of the northern part of the caldera, for which the InSAR image reveals the greatest deformation. The distance and orientation explanations in Figure 3a apply to all Figures in this composite. (b) HIPSHS model predictions. A deformation model simulating a spherical expansion source embedded within an HIPSHS accounts for 94% of the observed deformation. (c) Residual. The residual represents the difference between the predicted and observed InSAR image. (d) LOS displacement profile. Data (gray dots) extracted from the profile sector in Figure 3a are overlain by predictions (thin black curve) from Model A, loaded with the corresponding best fit parameters.

the origin, evolution, and composition of Okmok volcano. *Burgisser* [2005] provides a detailed analysis of the most recent caldera-forming eruption that occurred about 2400 years ago. The physiography resulting from this catastrophic event dominates the ongoing phase of the volcano's construction. Several cones dot the margins of the caldera, which was once entirely filled with water. Observed pillow lavas and other textures are consistent with subaerial eruptions within the caldera. The caldera lake breached the caldera along the northeast wall and has since diminished [*Miller et al.*, 1998b]. The most recent eruption began in February 1997 and continued through April of the same year. The interval was initiated by eruptions of steam and ash from cone A (Figure 2). Strombolian eruptions that began in mid-February [*Miller et al.*, 1998b] produced basaltic lava that flowed from cone A and crossed the caldera floor to the northeast [*Patrick et al.*, 2004].

[6] The InSAR data shown in Figure 3 span the 1997 eruption and capture the line-of-sight (LOS) deformation associated with the event. These data are taken from the work of *Lu et al.* [2005a], which includes a detailed

discussion of the InSAR acquisition and processing. An overview of the InSAR data is given here and summarized in Table 1. ERS-1 and ERS-2 satellites acquired descending-pass, C-band radar images of Okmok volcano in October 1995 and September 1997, respectively. The InSAR data constructed from this image pair suggest a radial pattern of subsidence having a maximum magnitude of about 1.5 m centered on the caldera. The co-eruption image actually spans a two-year interval that may include pre-eruption and posteruption behavior. Analyses of pre-eruption, co-eruption, and posteruption InSAR data for Okmok [*Lu et al.*, 2005a] indicate the deformation source is spatially stationary. Furthermore, the magnitudes of the estimated pre-eruption and posteruption deformation sources are an order of magnitude less than that of the co-eruption data. Therefore I assume the InSAR data shown in Figure 3 reflect only the co-eruption deformation. I chose to use Okmok volcano and the associated InSAR-observed co-eruption deformation as an example in this analysis for three reasons. First, the deformation predictions of a spherical expansion source are consistent with the radially symmetric deformation pattern suggested by the InSAR data [*Dzurisin*, 2003] (Figure 3). Second, several previous studies investigated observed deformation associated with the 1997 eruption of Okmok volcano and estimated the deformation source characteristics using models of a spherical expansion source embedded in an HIPSHS [*Lu et al.*, 1998, 2000a, 2005a; *Mann et al.*, 2002; *Miyagi et al.*, 2004]. Third, previous studies suggest the caldera of Okmok volcano may be relatively weak compared to the rest of the volcano [*Lu et al.*, 2005a; *Mann et al.*, 2002]. This inferred variation in material properties compels an assessment of the homogeneous material property distribution assumption, as well as a closer look at the implications of the combined suite of HIPSHS assumptions.

1.2. Standard Volcano Deformation Model

[7] A model is a simplified representation of a natural system. The reliability of model predictions depends on how well the model represents the natural system [*Wang and Anderson*, 1982]. Consequently, selecting an appropriate model is of paramount importance when conducting an analysis of deformation caused by magma intrusion. A spherical expansion source at depth can simulate the change in storage of a magma chamber and account for deformation caused by magma intrusion events [*Mogi*, 1958].

[8] The forward solution for a three component displacement vector, **u**, at point j on the free surface, caused by a spherical expansion source, s, embedded at ξ in a homogeneous, isotropic, elastic half-space, is

$$\mathbf{u}_j = s\mathbf{u}_j^*, \text{and } \mathbf{u}_j^* = \left[(x-\xi_x),\left(y-\xi_y\right),(-\xi_z)\right]/R^3, \qquad (1)$$

where R is the Euclidean distance from ξ to j [e.g., *Lu et al.*, 2002c] and z is orthogonal to the free-surface and upward-positive (Figure 1). For a given geometric configuration, the predicted displacement at the free surface is a linear function of the expansion source strength. The expansion source strength can be expressed in terms of either a change in volume, ΔV, of the sphere or a change of pressure, ΔP, along the surface of the sphere

$$s = \Delta V\frac{(1-\nu)(1+\nu)}{2\pi(1-2\nu)} = \Delta P(1-\nu)\frac{r_s^3}{G}, \qquad (2)$$

where ν is Poisson's ratio, r_s is the radius of the sphere, G is the shear modulus, and expansion is positive [*Trasatti et al.*, 2005]. For the case of $\nu = 0.25$, a radial coordinate system (r, z), and an expansion source expressed in terms of ΔP located along the axis of radial symmetry, the relationships given in equations (1) and (2) reduce to the expression given by *Mogi* [1958]:

$$\begin{aligned} u_r &= \frac{3r_s^3\Delta P}{4G}\frac{r}{R^3} \\ u_z &= \frac{3r_s^3\Delta P}{4G}\frac{(-z)}{R^3}, \end{aligned} \qquad (3)$$

where u_r and u_z are radial and vertical displacements, respectively, and $(-z)$ is the depth to the expansion source. The allure of *Mogi*'s [1958] model lies in its combination of computational simplicity and remarkable ability to precisely predict radially symmetric deformation caused by magma intrusion events. However, the accuracy of an interpretation based on *Mogi*'s [1958] model is subject to the validity of the HIPSHS assumptions, an often overlooked consideration.

1.3. HIPSHS Assumptions

[9] The half-space assumption implies the land surface is flat. However, the total relief within a local region surrounding a volcano can be several kilometers. Others suggested that errors associated with the half-space assumption are predictable and may be significant [e.g., *Cayol and Cornet*, 1998; *Gottsmann et al.*, 2006a]. *Williams and Wadge* [1998] propose a simple first-order correction, for which the depth to the expansion source for each computational displacement point is adjusted for the difference between actual and reference elevations. *Williams and Wadge* [2000] expand this simple scheme to include higher-order and more precise topographic corrections. Displacement predictions generated using the higher-order correction scheme agree with FEM-generated synthetic deformation predictions better than predictions generated using the simpler first-order topographic correction scheme. However, owing to its simplicity, the first-order correction scheme is commonly applied in analyses of volcano deformation [e.g., *Lundgren et al.*, 2003].

[10] The Poisson's ratios for typical crustal rocks are $0.1 < \nu < 0.4$ [*Turcotte and Schubert*, 1982]. Bulk crustal representations are $0.25 < \nu < 0.32$ [*Christensen*, 1996] and may

Table 1. InSAR Image[a]

	Satellite	Orbit	Acquisition Date	Track	Baseline, m	LOS [East, North, Up]
Image 1	ERS-1	22147	9 Oct. 1995	115	8	[0.346, −0.081, 0.935]
Image 2	ERS-2	12494	9 Sept. 1997			

[a] InSAR, Interferometric synthetic aperture radar; LOS, line of sight.

be appropriate for volcano-wide deformation assessments, which have spatial scales of a few tens of kilometers. The Poisson-solid assumption ($\nu = 0.25$) represents the lower bound of this range, rather than the bulk average. On the basis of equation (2), the relative displacement predictions for the expansion source, embedded in a homogeneous and isotropic half-space, differ by about 30% for $\nu = 0.25$ versus $\nu = 0.32$. The presence of pore fluids, which exist in the crust to depths of several kilometers [*Nur and Walder*, 1992], exacerbates the sensitivity to the Poisson-solid assumption. The short time response to a rapid loading event in a poroelastic system is undrained. Subsequently, the system will converge to drained conditions as excess pore pressure decays to equilibrium. Undrained conditions reflect a relatively stiff behavior with respect to the drained counterpart. For analyses of deformation, the choice of material properties to represent the crust must therefore account for the poroelastic state of the system. Relationships for drained and undrained values of Poisson's ratio, ν and ν_u respectively, are

$$\nu = \frac{3\nu_u - \alpha B(1+\nu_u)}{3 - 2\alpha B(1+\nu_u)} \text{ and } \nu_u = \frac{3\nu + \alpha B(1-2\nu)}{3 - \alpha B(1-2\nu)}, \quad (4)$$

where B is Skempton's coefficient and α is the Biot-Willis parameter [*Wang*, 2000]. Using equation (2) and the drained and undrained Poisson's ratios for Westerly Granite, $\nu = 0.25$ and $\nu = 0.34$ respectively [*Wang*, 2000], displacement predictions differ by about 40%. This difference is significant, with respect to expected measurement uncertainties for GPS and InSAR, for co-eruptive deformation signals having magnitudes of more than a few centimeters.

[11] Recent studies of deformation of Aleutian volcanoes [*Lu et al.*, 2002c, 2003b, 2005a] abandoned the Poisson-solid assumption and instead use specifications based on laboratory petrophysical data [*Christensen*, 1996]. When available, field data for volcanoes are discordant with the Poisson-solid assumption. For example, a seismic tomography study of the Hengill-Grensdalur volcanic complex in Iceland [*Miller et al.*, 1998a] revealed a spatial distribution of V_P/V_S ratios, from which estimations for Poisson's ratio are calculated [*Christensen*, 1996]:

$$\nu = \frac{1}{2}\left[1 - \frac{1}{(V_P/V_S)^2 - 1}\right] \text{and } V_P/V_S = \sqrt{1 + \frac{1}{1-2\nu}}. \quad (5)$$

The results given by *Miller et al.* [1998a] suggest that Poisson's ratio varies from $0.23 \le \nu \le 0.29$, which includes the special case of $\nu = 0.25$, over a 5-km-thick, 20 km × 20 km region of the Hengill-Grensdalur volcanic complex. However, these variations over the problem domain not only suggest that the Poisson-solid assumption may be invalid, but that the assumption of a homogeneous material property distribution is also invalid for that particular example.

[12] Direct measurements of crustal anisotropy below volcanoes are sparse. However, the near surface and flank structure of a volcano is arguably best described as a layered system of successively emplaced erupted materials. This structure agrees with the alternating lava and pyroclastic layers of Okmok volcano that is suggested by *Miller et al.* [1998b], as well as the observed volcano-wide stratified facies deposited as a result of the most recent caldera-forming eruption [*Burgisser*, 2005]. This layering translates to anisotropy at some scale, such that stiffness in the lateral directions is different than that of the vertical direction. Alternatively, vertical fracture systems resulting from regional or local stress regimes of the Aleutian Arc subduction zone [e.g., *Lu et al.*, 2005b; *Singer et al.*, 1992; *Zoback*, 1992] imply anisotropic material properties. In these cases, the elastic properties will be compliant and stiff in directions normal and parallel, respectively, to the fracture systems. In any case, it is reasonable to expect that a volcano system will have anisotropic elastic properties.

[13] Volcano structure involves sequences of deposition and emplacement of various materials; magma intrusion, crystallization, and alteration; fracture systems; and shallow hydrothermal systems. Conceptual models of volcanic structure (based on field observations, seismic tomography, and geochemical data) do not concur with the assumption of homogeneous material properties at a volcano-wide scale. Compilations of material properties derived from laboratory experiments are readily available for a variety of rocks types and compositions [e.g., *Birch*, 1960; *Christensen and Mooney*, 1995; *Christensen*, 1996; *Wang*, 2000]. In the absence of material property data for a particular volcano of interest, reasonable material property specifications can be extracted from these compilations.

2. Method

[14] Prediction sensitivities to the HIPSHS assumptions are revealed by assessing the observed InSAR data that map deformation of the 1997 eruption of Okmok volcano, Alaska, using both forward and inverse models. Sensitivities of deformation predictions to the individual assumptions are systematically isolated and quantified by loading forward spherical expansion source non-HIPSHS models with the spherical expansion source parameters estimated using the HIPSHS model. For the inverse modeling analysis, matrices of both analytical and FEM-generated impulse response functions (IRFs) are combined with standard inverse methods to isolate and reveal the influence of each HIPSHS assumption on the estimations of both linear and nonlinear expansion source parameters. The estimated parameters are then compared to those of the reference HIPSHS model. The various models considered in this study are summarized in Table 2.

2.1. Analytical Solutions

[15] A reference model (Model A) is defined for a three-dimensional problem domain having east, north, and up Cartesian coordinate axes with the origin collocated with the northwest corner of the InSAR image (Figure 3a). Expressed in matrix notation, the forward model of equation (1) for displacement due to an expansion source is

$$\mathbf{G}^{\mathrm{A}} s^{\mathrm{A}} = \mathbf{d}, \quad (6)$$

where $\mathbf{G}^{\mathrm{A}}$ is a column vector of IRFs for LOS displacement due to a unit-strength spherical expansion source, s^{A} is the strength of the spherical expansion source, and $\mathbf{d}$ is a column vector of InSAR-observed displacements. Each

Table 2. Model Configurations[a]

Model	Impulse Response Function	Class	Relaxed Assumption	Specifications
A	$\mathbf{G}^{\mathrm{A}}$	analytical	none	free surface: flat $\nu = 0.25$, $G = 15$ GPa
B	$\mathbf{G}^{\mathrm{B}}$	analytical	half-space	free surface: topography $\nu = 0.25$, $G = 15$ GPa
C	$\mathbf{G}^{\mathrm{C}}$	analytical	Poisson-solid	free surface: flat $\nu = 0.34$, $G = 15$ GPa
FA	$\mathbf{G}^{\mathrm{FA}}$	numerical	none	free surface: flat $\nu = 0.25$, $G = 15$ GPa
D	$\mathbf{G}^{\mathrm{D}}$	numerical	isotropy	free surface: flat $\mathbf{M}$ (stiffness tensor), GPa $\begin{vmatrix} 53.62 & 14.08 & 11.41 & 0 & 0 & 0 \\ 14.08 & 53.62 & 11.41 & 0 & 0 & 0 \\ 11.41 & 11.41 & 43.95 & 0 & 0 & 0 \\ 0 & 0 & 0 & 14.63 & 0 & 0 \\ 0 & 0 & 0 & 0 & 19.77 & 0 \\ 0 & 0 & 0 & 0 & 0 & 19.77 \end{vmatrix}$
E	$\mathbf{G}^{\mathrm{E}}$	numerical	homogeneity	free surface: flat upper crust: $\nu = 0.25$, $G = 15.0$ GPa lower crust: $\nu = 0.29$, $G = 77.8$ GPa mantle: $\nu = 0.27$, $G = 100.8$ GPa
F	$\mathbf{G}^{\mathrm{F}}$	numerical	homogeneity	free surface: flat shallow caldera: $\nu = 0.25$, $G = 1.0$ GPa upper crust: $\nu = 0.25$, $G = 15.0$ GPa lower crust: $\nu = 0.29$, $G = 77.8$ GPa mantle: $\nu = 0.27$, $G = 100.8$ GPa
G	$\mathbf{G}^{\mathrm{G}}$	numerical	homogeneity	free surface: flat caldera: $\nu = 0.25$, $G = 7.5$ GPa upper crust: $\nu = 0.25$, $G = 15.0$ GPa lower crust: $\nu = 0.29$, $G = 77.8$ GPa mantle: $\nu = 0.27$, $G = 100.8$ GPa
H	$\mathbf{G}^{\mathrm{H}}$	numerical	homogeneity	free surface: flat shallow caldera: $\nu = 0.25$, $G = 1.0$ GPa caldera: $\nu = 0.25$, $G = 7.5$ GPa upper crust: $\nu = 0.25$, $G = 15.0$ GPa lower crust: $\nu = 0.29$, $G = 77.8$ GPa mantle: $\nu = 0.27$, $G = 100.8$ GPa

[a] The configuration for Model B includes the topography correction suggested by *Williams and Wadge* [1998]. The transversely isotropic stiffness tensor for Model D [*Godfrey et al.*, 2000] is rotated, such that the slow axis is parallel to the model axis of symmetry and scaled to satisfy $K = K^*$ (see equation (11)).

element, $\mathbf{G}_j^{\mathrm{A}}$, is the predicted displacement for position j projected onto the LOS vector, $\mathbf{n}$:

$$\mathbf{G}_j^{A} = \mathbf{u}_j^{*} \bullet \mathbf{n}, \qquad (7)$$

where $\mathbf{u}_j^{*}$ is a vector of three-component displacements calculated using equation (1). The relationship is further conditioned to allow for a plane superposed on the deformation field. This plane accounts for phase ramping in the InSAR image caused by uncertainties in the satellite positions [*Massonnet and Feigl*, 1998]. The matrix of IRFs in equation (7) is appended with column vectors corresponding to the pixel positions (**x** and **y**) and a unity vector. The coefficients for the vertical projection of a plane are appended to s^{A} and form the source vector, $\hat{\mathbf{s}}$:

$$\hat{\mathbf{G}}\hat{\mathbf{s}} = \mathbf{d}, \text{where } \hat{\mathbf{G}} = \left[\mathbf{G}^{\mathrm{A}}(\mathbf{x}\ \mathbf{y}\ \mathbf{1})n_z\right] \text{and } \hat{\mathbf{s}} = \begin{pmatrix} s^{\mathrm{A}} \\ a \\ b \\ c \end{pmatrix}, \qquad (8)$$

where n_z is the vertical component of the LOS basis vector.

[16] I take advantage of the radial symmetry of the deformation pattern suggested by the InSAR data and assume the horizontal location of the source is near the center of the caldera, in accord with earlier analyses [*Lu et al.*, 1998, 2000a, 2005a; *Mann et al.*, 2002; *Miyagi et al.*, 2004] (Figure 3). Following the method described by *Lu et al.* [2003b, 2005a], an inverse modeling scheme simultaneously estimates the two parameters and uncertainties of the expansion source (ξ_z and s^{A}), as well as the plane coefficients (a, b, and c). The scheme uses Monte Carlo simulations of the downhill simplex method [*Press et al.*, 1992] that minimize the root-mean-squared-error (RMSE) of displacement predictions.

[17] Results suggest the depth of the expansion source is about 3.1 km beneath the land surface (Figure 4), a depth that corresponds to the neutral buoyancy for basaltic magma [*Dvorak and Dzurisin*, 1997] and is consistent with other analyses of both InSAR and GPS data [*Lu et al.*, 2000a, 2005a; *Mann et al.*, 2002; *Miyagi et al.*, 2004]. The estimated pressure of the source is −270 MPa. The magnitude of this result is about 200 MPa greater than lithostatic stress and conceptually problematic. The implications of this result are revisited in the discussion. The reference

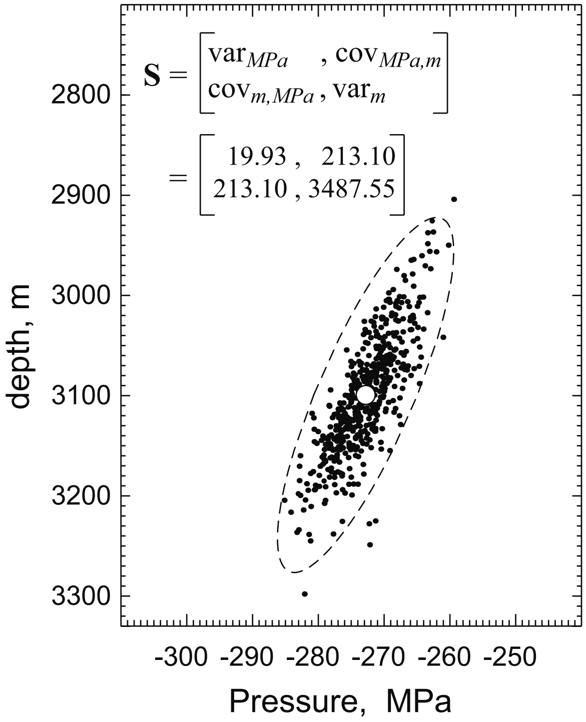

Figure 4. Estimated pressure and depth parameters of the spherical expansion source, Model A. Each point represents one root-mean-squared-error (RMSE) best fit estimate for each of the 500 realizations of the InSAR data. **S** is the correlation matrix [*Davis*, 2002] of the estimated pressure and depth parameters. The dashed ellipse is the 99% confidence interval constructed from a principal component analysis of **S**. The white circle at the center of the ellipse is the first moment of the distribution and the assumed source for Model A. The orientation of the ellipse reveals the coupling of depth and pressure estimates.

model is the product $\mathbf{G}^{\mathrm{A}}s^{\mathrm{A}}$ for $\nu = 0.25$ and the deformation source location of ξ. This simple model predicts 94% of the observed deformation.

[18] Model B tests the sensitivity to the half-space assumption. This model consists of the column vector of IRFs, $\mathbf{G}^{\mathrm{A}}$, corrected for topographic effects using the method given by *Williams and Wadge* [1998] and the DEM shown in Figure 2. The resulting vector, $\mathbf{G}^{\mathrm{B}}$, is scaled by s^{A}. Model C tests the sensitivity to the Poisson-solid assumption. This model consists of the column vector of IRFs, $\mathbf{G}^{\mathrm{A}}$, which are scaled by β, to simulate a non-Poisson solid. The relationship is $\mathbf{G}^{\mathrm{C}} = \beta\mathbf{G}^{\mathrm{A}}$, where

$$\beta = \left[\frac{(1-\nu_2)(1+\nu_2)}{(1-2\nu_2)}\right]\left[\frac{(1-\nu_1)(1+\nu_1)}{(1-2\nu_1)}\right]^{-1} \tag{9}$$

is the ratio of equation (2) for a non-Poisson-solid (ν_2) to a Poisson-solid (ν_1) determined by holding s^{A} and ΔV constant. Predictions of $\mathbf{G}^{\mathrm{C}}s^{\mathrm{A}}$ are compared to the reference model to reveal the sensitivity to the Poisson-solid assumption.

2.2. Finite Element Models

[19] The two governing equations that describe an elastic material for an axisymmetric problem domain are

$$\begin{aligned} G\left(\frac{\partial^2 u_r}{\partial r^2} + \frac{1}{r}\frac{\partial u_r}{\partial r} - \frac{u_r}{r^2} + \frac{\partial^2 u_r}{\partial z^2}\right) + \frac{G}{1-2\nu}\frac{\partial \varepsilon}{\partial r} = 0 \\ G\left(\frac{\partial^2 u_z}{\partial r^2} + \frac{1}{r}\frac{\partial u_z}{\partial r} - \frac{u_z}{r^2} + \frac{\partial^2 u_z}{\partial z^2}\right) + \frac{G}{1-2\nu}\frac{\partial \varepsilon}{\partial z} = 0 \end{aligned}, \tag{10}$$

where ε is the volumetric strain [*Wang*, 2000]. The solution for a spherical expansion source in an HIPSHS [e.g., *Mogi*, 1958] satisfies these governing equations. Alternatively, FEMs can solve these governing equations over various problem domain configurations, subject to any desired combination (including none) of the HIPSHS assumptions.

[20] All FEMs in this study are constructed with the finite element code *ABAQUS* (available at www.abaqus.com) and share several configuration characteristics. Each FEM simulates a pressurized spherical inclusion within a three-dimensional domain that is symmetric about a vertical axis located near the simulated center of the caldera. Similar FEM configurations are used in studies of the axisymmetric structure and deformation patterns of Campi Flegrei caldera [*Trasatti et al.*, 2005; *Troise et al.*, 2003]. The top of the problem domain is a flat free surface. The bottom and lateral boundaries are specified zero-displacement and are located relatively far away from the simulated caldera. Problem domains are tessellated with quadrilateral elements having bilinear interpolation. LOS displacement predictions are generated by sweeping the extracted nodal displacement predictions, $u|_{(z=0)}$, about the axis of symmetry and projecting the results on the LOS basis vector.

[21] The FEM, Model FA having IRFs $\mathbf{G}^{\mathrm{FA}}$, simulates a spherical expansion source buried in an HIPSHS. The differences between predictions from $\mathbf{G}^{\mathrm{FA}}s^{\mathrm{A}}$ and $\mathbf{G}^{\mathrm{A}}s^{\mathrm{A}}$ are a combination of the errors associated with the tessellated approximation of the finite problem domain and the errors associated with the finite spherical cavity of the FEM versus the analytical solution (Figure 5), which assumes the sphere is very small. Sensitivity analyses to the tessellation density suggest the slightly more peaked shape of the FEM displacement predictions is due to the neglect of higher-order terms in the point-source assumption of the analytical solution [*McTigue*, 1987]. However, the differences are relatively subtle; for simulated source radii of 500 and 1000 m, the volcano-wide residual LOS image of $\mathbf{G}^{\mathrm{FA}}s^{\mathrm{A}} - \mathbf{G}^{\mathrm{A}}s^{\mathrm{A}}$ is less than one fringe and two fringes, respectively. The respective magnitudes of pressurization required to predict the observed deformation are on the order of 10^8 to 10^9 Pa. Pressures required for the 500-m-radius spherical source grossly exceed lithostatic conditions and the assumed radius for the pressurized spherical inclusion is 1000 m. The FEM configuration for Model FA serves as a base configuration that is modified as necessary to construct the various non-HIPSHS FEM configurations. The residual from the HIPSHS model, 1.1 cm (Figure 3 and Table 3), represents a specified upper limit of allowable misfit for prediction differences of the alternatives versus the HIPSHS model. The RMSE of $\mathbf{G}^{\mathrm{FA}}s^{\mathrm{A}} - \mathbf{G}^{\mathrm{A}}s^{\mathrm{A}}$ (0.4 cm) is much less than that of $\hat{\mathbf{G}}\,\hat{\mathbf{s}} - \mathbf{d}$ (1.1 cm) and comparison of Figures 3c to Figures 5b and 5c indicates that Model FA is a valid

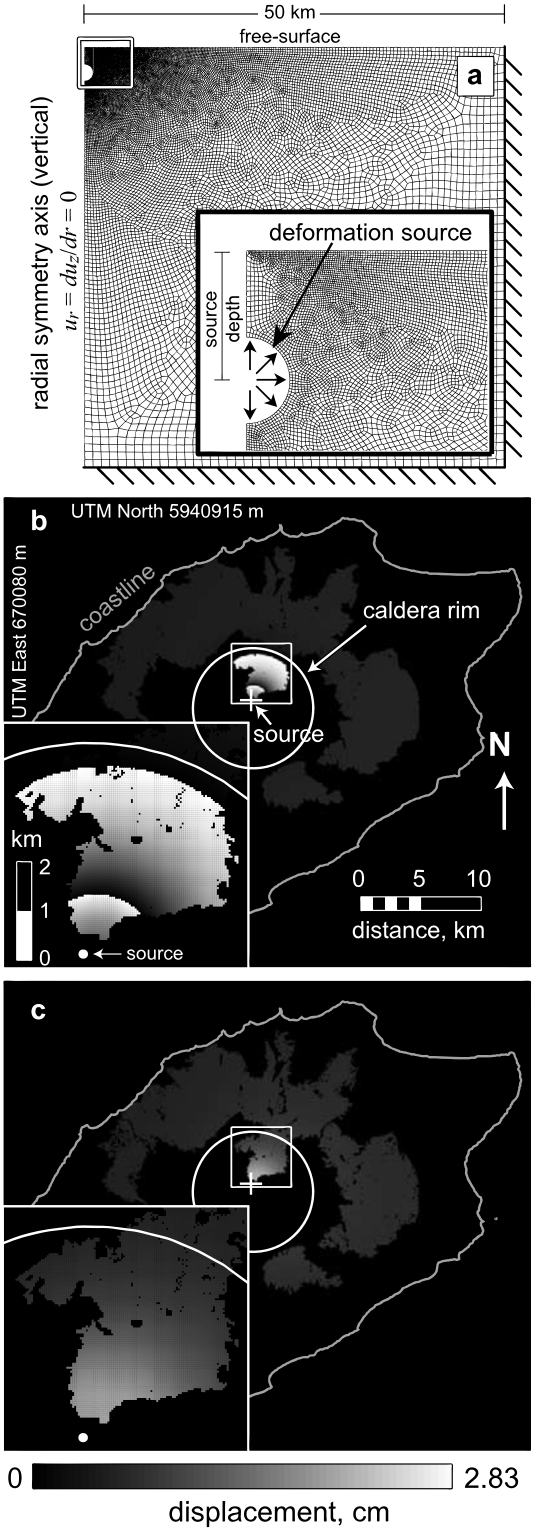

Figure 5. Finite element model (FEM) validation. (a) Axisymmetric FEM mesh and configuration. This configuration is designed to simulate an expansion source embedded in an HIPSHS. The problem domain is tessellated into 18,142 elements. (b) Forward model residual ($\mathrm{G}^{\mathrm{FA}}s^{\mathrm{A}} - \mathrm{G}^{\mathrm{A}}s^{\mathrm{A}}$), r_s = 1000 m. (c) Forward model residual ($\mathbf{G}^{\mathrm{FA}}s^{\mathrm{A}} - \mathbf{G}^{\mathrm{A}}s^{\mathrm{A}}$), r_s = 500 m. Each fringe, black-gray-white, represents 2.83 cm of deformation parallel to the LOS vector and toward the satellite for Figures 5b and 5c.

representation of a spherical expansion source embedded in an HIPSHS (Model A).

[22] The second FEM, Model D having IRFs $\mathbf{G}^{\mathrm{D}}$, relaxes the isotropy assumption. A transversely isotropic stiffness tensor, **M**, is specified for the entire problem domain (Table 2). The tensor is rotated into the model coordinate system such that the compliant (slow) axis is aligned with the axis of symmetry. This configuration simulates the interbedded structure of lava flows and volcaniclastic deposits commonly associated with volcanoes [e.g., *Stern*, 2002]. In order to make a valid comparison between predictions from $\mathbf{G}^{\mathrm{FA}}s^{\mathrm{A}}$ and $\mathbf{G}^{\mathrm{D}}s^{\mathrm{A}}$, the stiffness tensor, determined from laboratory experiments on Chugach phyllite [*Godfrey et al.*, 2000], is scaled such that the generalized bulk modulus, K^*, of the transversely isotropic stiffness tensor [*Cheng*, 1997] is equivalent to the bulk modulus, K, of the isotropic material specified for $\mathbf{G}^{\mathrm{FA}}$:

$$K = K^* = \frac{\mathbf{M}_{iijj}}{9}. \tag{11}$$

[23] This configuration is not intended to imply that the volcano consists of Chugach phyllite. Rather, this configuration serves two purposes. First, it allows me to assess the significance of a moderate level (~10%) of elastic anisotropy on deformation predictions. Second, it demonstrates that the effects of elastic anisotropy are readily simulated in both forward and inverse models of volcano deformation. Although I use transverse isotropy to capitalize on the apparent symmetry of this particular natural system, one can populate and rotate stiffness tensors to simulate distributions of general elastic anisotropy in three-dimensional deformational systems [e.g., *Masterlark*, 2003].

[24] A series of FEMs are developed to simulate four different types of heterogeneous configurations, which are summarized in Table 2 and illustrated in Figure 6. Model E, having IRFs $\mathbf{G}^{\mathrm{E}}$, simulates a system of crustal-scale horizontal layers having different elastic properties (a layered half-space). This deviation from the complete set of HIPSHS assumptions is occasionally used in models of volcano deformation [e.g., *Pritchard and Simons*, 2002]. The layered configuration follows the velocity structure of the Aleutian arc, determined using field [*Fliedner and Klemperer*, 1999] and complementary laboratory [*Christensen*, 1996] data.

[25] The collapse during the most recent caldera-forming eruption [*Burgisser*, 2005] implies that the material within the caldera is weakened, with respect to the flanks of the volcano. Models F, G, and H (having IRFs $\mathbf{G}^{\mathrm{F}}$, $\mathbf{G}^{\mathrm{G}}$, $\mathbf{G}^{\mathrm{H}}$) include various weak caldera configurations that are embedded in the layered configuration of Model E. These embedded calderas provide problem domains having both vertical and horizontal heterogeneity. The configuration of Model F includes a thin and weak layer blanketing the caldera floor and simulates the weak shallow substrate suggested by others to account for observed subsidence of newly emplaced lava flows [*Briole et al.*, 1997; *Lu et al.*, 2005a; *Stevens et al.*, 2001]. Model G simulates a moderately weak material throughout the caldera. The configuration of Model H simulates a moderately weak caldera, overlain by a thin weak layer, and is arguably the most

Table 3. Residual, Forward Models[a]

Difference	Figure	RMSE, mm	Residual Fringes	Percentage of Reference Signal
$\hat{\mathbf{G}}\,\hat{\mathbf{s}} - \mathbf{d}$	3c	11.0	2+	93.5
$\mathbf{G}^{B}s^{A} - \mathbf{G}^{A}s^{A}$	7a	2.9	<1	98.2
$\mathbf{G}^{C}s^{A} - \mathbf{G}^{A}s^{A}$	7b	82.7	17+	52.6
$\mathbf{G}^{FA}s^{A} - \mathbf{G}^{A}s^{A}$	5b	4.4	1+	96.2
$\mathbf{G}^{FA}s^{A} - \mathbf{G}^{A}s^{A}$	5c	4.4	<1	95.5
$\mathbf{G}^{D}s^{A} - \mathbf{G}^{FA}s^{A}$	8	21.4	8+	88.7
$\mathbf{G}^{E}s^{A} - \mathbf{G}^{FA}s^{A}$	9a	10.5	<1	88.0
$\mathbf{G}^{F}s^{A} - \mathbf{G}^{FA}s^{A}$	9b	23.1	10+	83.5
$\mathbf{G}^{G}s^{A} - \mathbf{G}^{FA}s^{A}$	9c	127.4	>20	64.3
$\mathbf{G}^{H}s^{A} - \mathbf{G}^{FA}s^{A}$	9d	168.9	>20	54.1

[a] For $\mathbf{G}^{B}s^{A} - \mathbf{G}^{A}s^{A}$, topographic corrections are calculated with respect to the elevation (409 m) of the horizontal position of the source(ξ_x, ξ_y). The spherical expansion source radii for the first and second instances of $\mathbf{G}^{FA}s^{A} - \mathbf{G}^{A}s^{A}$, are 1000 m and 500 m, respectively.

realistic representation of Okmok volcano among the models considered in this study. Field and theoretical studies [e.g., *Gudmundsson and Loetveit*, 2005] demonstrate that magma migrates upward through dikes until it encounters an interface with a weak layer. The conceptual magma chambers for Models G and H are thus chosen to occupy the mechanical discontinuity separating the stiff upper crust from the overlying weak caldera. This configuration is in accord with other FEM-based studies of heterogeneous volcano deformation systems [*Trasatti et al.*, 2003, 2005].

3. Results

3.1. Forward Models

[26] Comparisons between predictions from non-HIPSHS and HIPSHS IRFs loaded with the best fit source, s^{A} (Figure 4),

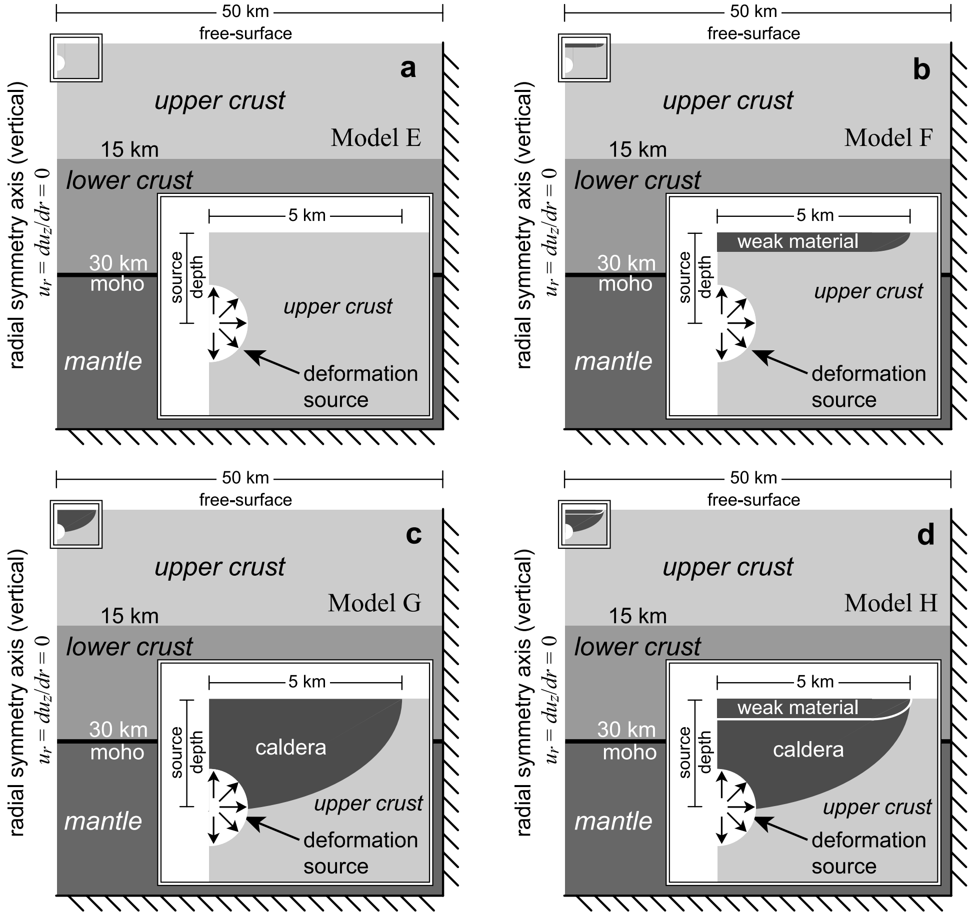

Figure 6. Relaxing the homogeneous assumption: FEM configurations. (a) Model E, simple regional-scale layered half-space. (b) Model F, thin, weak layer overlying the caldera; embedded in a layered half-space. (c) Model G, moderately weak caldera; embedded in a layered half-space. (d) Model H, thin, weak layer overlying a moderately weak caldera; embedded in a layered half-space.

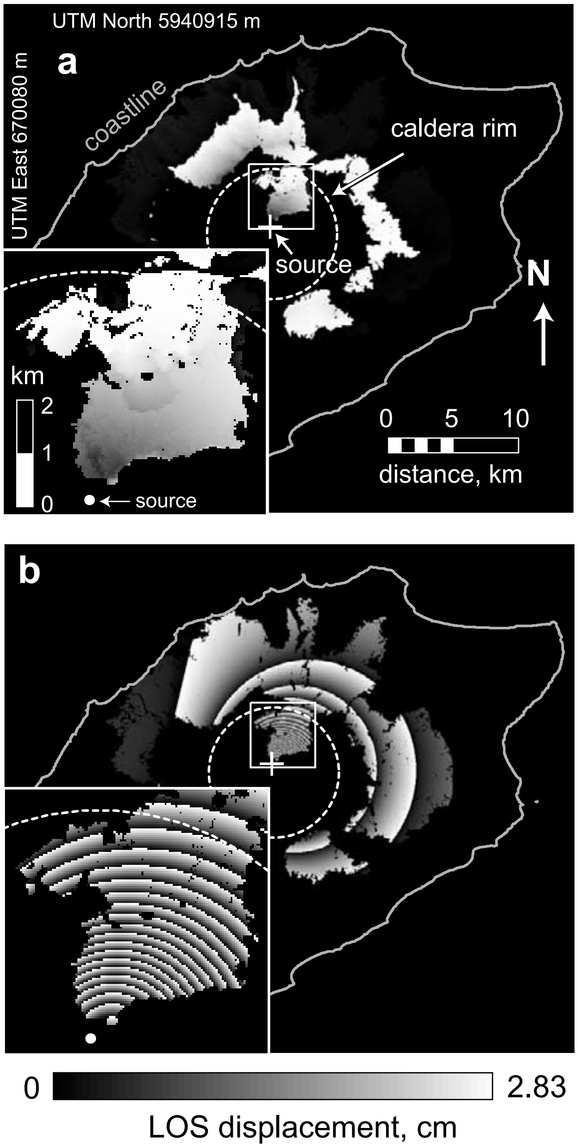

Figure 7. Sensitivities to corrections for the analytical solution of *Mogi* [1958]. Each fringe, black-gray-white, represents 2.83 cm of deformation parallel to the LOS vector and toward the satellite. (a) Forward model residual ($\mathbf{G}^{B}s^{A} - \mathbf{G}^{A}s^{A}$): sensitivity to topographic effects for a reference elevation of 409 m above mean sea level. The reference elevation is the elevation of the horizontal position of the HIPSHS source. Topographic effects are minimal within coherent portions of the InSAR image. (b) Forward model residual ($\mathbf{G}^{C}s^{A} - \mathbf{G}^{A}s^{A}$): sensitivity to the Poisson-solid assumption. Deformation from this configuration overestimates that of the reference model.

reveal sensitivities to each of the HIPSHS assumptions. Synthetic LOS residual images, constructed from the differences between the observed InSAR data and predictions, are usually presented to justify and assess the suitability of a particular deformation model [e.g., *Lu et al.*, 2005a; *Wicks et al.*, 2002]. Accordingly, in this study, comparisons between reference and alternative models are expressed as RMSE, as well as differences between the LOS predictions. Forward model results are summarized in Table 3.

[27] The predictions of $\mathbf{G}^{A}s^{A}$ represent the reference model, to which predictions from alternative models relaxing the half-space (Model B) and Poisson-solid (Model C) assumptions are compared (Figure 7). Okmok is a shield volcano and topographic gradients are relatively small. Topographic effects, or the implications of the deviations from the assumed flat surface of the problem domain, are minimal. Predicted deformation from $\mathbf{G}^{B}s^{A}$ recovers 98% of the deformation predicted by $\mathbf{G}^{A}s^{A}$. Prediction differences ($\mathbf{G}^{B}s^{A} - \mathbf{G}^{A}s^{A}$) have an RMSE of 3 mm and reveal less than one interferometric fringe over the InSAR data footprint.

[28] Laboratory experiments for crystalline rocks [*Christensen*, 1996] suggest the Poisson-solid assumption underestimates the expected Poisson's ratio for basalt, the principal rock type of Okmok volcano. More realistic higher values of Poisson's ratio for the problem domain can have a significant impact on forward model predictions. Predicted deformation from $\mathbf{G}^{C}s^{A}$ recovers only 53% of the deformation predicted by $\mathbf{G}^{A}s^{A}$. Prediction differences ($\mathbf{G}^{C}s^{A} - \mathbf{G}^{A}s^{A}$) have a RMSE of 83 mm and reveal more than 17 interferometric fringes over the InSAR data footprint. The magnitude of these systematic prediction differences suggests the Poisson-solid assumption must be carefully considered when designing a conceptual model of volcano deformation.

[29] The predictions of $\mathbf{G}^{FA}s^{A}$ represent an FEM-based reference model, to which predictions from alternative FEMs relaxing the isotropic (Model D) and homogeneous (Models E, F, G, and H) assumptions are compared. The implications of the isotropic material properties assumption are significant. For the configuration tested (Model D), which simulates transverse isotropy having stiff directions in the horizontal plane, the predicted deformation has a flattened peak of about eight fringes in the caldera region (Figure 8). The sensitivities of forward modeling predictions to deviations from the homogeneous distribution of material properties depend heavily on the particular heterogeneous configuration (Figure 9). For the layered model (Model E), the prediction differences were negligible. Augmenting the layered model with a thin layer of weak material overlying the caldera (Model F) overpredicts the deformation in the caldera region by about 10 fringes in the caldera region. Forward model predictions from Model G, a moderately weak caldera embedded in the simple layered configuration of Model E, substantially overestimate subsidence in the caldera region. Forward model predictions from Model H, which includes the combined complexity of the three preceding heterogeneous models, severely overestimate subsidence of the caldera region by more than 20 fringes. Figure 10 summarizes the forward modeling predictions from various model configurations with respect to the work of *Mogi* [1958], assuming the constant source strength and depth, s^{A}, shown in Figure 4.

3.2. Inverse Models

[30] Inverse analyses utilizing FEM-generated IRFs are the most innovative part of this study. Deformation predictions are nonlinear functions of the depths of the simulated spherical expansion sources. These functions are linearized by constructing a series of FEMs, for which the source depth is perturbed by 100-m increments over depths ranging

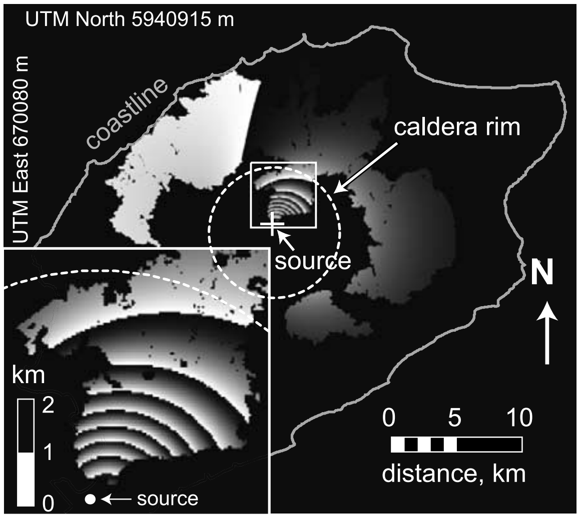

Figure 8. Forward model residual ($\mathbf{G}^{D}s^{A} - \mathbf{G}^{FA}s^{A}$): sensitivity to the isotropy assumption. Each interferometric fringe, black-gray-white, represents 2.83 cm of deformation parallel to the LOS vector and toward the satellite. Deformation from this configuration has a flattened shape and underestimates the deformation of the reference model.

from 2500–5000 m. A total of 132 FEMs are constructed for this analysis; 26 FEMs for each of the numerical model configurations D through H listed in Table 2 and two additional FEMs to generate IRFs $\mathbf{G}^{FA}$ for spherical expansion sources having radii of 500 and 1000 m, respectively. Construction of each FEM requires about 15 min and run times are negligible. An algorithm was developed to extract nodal displacements from an individual model, assemble the IRF matrix, substitute the matrix into equation (8), and solve for the least-squares estimates of the source parameters. The algorithm is constructed to automatically execute this procedure for all the FEMs. Results are summarized in Figure 11 and Table 4. Residual images are shown in Figure 12.

[31] The bulk misfit, RMSE ~1 cm, is robust among the models considered in the inverse analysis, although the depth and pressure estimates of the source for some of the alternative models that simulate heterogeneous material properties deviate significantly from those of the HIPSHS model. Estimated parameters for the simple layered configuration are very similar to those of the HIPSHS model. As demonstrated in the forward modeling analysis, topographic effects are minimal for the models and data considered in this study. Both equation (2) and the forward modeling analysis suggest that predictions are sensitive to the choice of Poisson's ratio. However, because equation (2) is independent of depth, only the magnitude of the estimated source will vary from the source characteristics estimated by inverting $\mathbf{G}^{A}$, because $\mathbf{G}^{C} = \beta\mathbf{G}^{A}$. Therefore neither Model B nor Model C is considered in the inverse analysis.

[32] The estimated source parameters for the model that relaxes the isotropic assumption, IRFs $\mathbf{G}^{D}$, suggest the source, s^{D}, is shallower and has a larger magnitude than that of the HIPSHS model. Both of these characteristics are significantly different (99% confidence) from those for s^{A}, the HIPSHS reference model. Estimated source parameter errors associated with the homogeneous material property assumption depend on the specific heterogeneous configuration. Source parameters, s^{E}, for a heterogeneous configuration representing regional-scale layering, IRFs $\mathbf{G}^{E}$, are not significantly different from those of the HIPSHS reference model. The three remaining models (IRFs $\mathbf{G}^{F}$, $\mathbf{G}^{G}$, and $\mathbf{G}^{H}$) simulate configurations of local heterogeneity associated with the caldera. Results indicate that estimated sources are significantly different (99% confidence) from those of the reference model. This explains why the forward modeling analysis indicates that the homogeneous assumption produces the greatest prediction errors if the true system has a weak caldera. The inverse models suggest that the relatively weak caldera configuration forces the source to be much deeper than that of the reference model (Figure 11). A similar but more qualitative result was obtained by *Bianchi et al.* [1987] and *Trasatti et al.* [2005] for Campi Flegrei caldera.

4. Discussion

[33] Model A, the spherical expansion source embedded in an HIPSHS [*Mogi*, 1958] provides a suitable fit to the InSAR data. In the absence of information other than the InSAR data, Model A is the preferred model because it is the simplest model and fits the InSAR data as well as the more complex models considered in this analysis. However, although Okmok is a relatively poorly studied volcano because of its remote location, the available and analog information for Okmok indicates that none of the HIPSHS assumptions are valid. Therefore interpretations based on the results of the HIPSHS model must be tempered by the validity (or invalidity) of model assumptions. None of the models presented here adequately represent the natural system of Okmok volcano. However, each alternative model simulates a natural complexity, for which the combined suite of HIPSHS assumptions cannot account for.

[34] The forward models systematically relax and isolate the prediction errors attributed to each of the HIPSHS assumptions. On the basis of the models considered in this study, of all the HIPSHS assumptions, deformation predictions were least sensitive to topographic effects. Topographic effects are insignificant if the reference elevation is chosen as the elevation corresponding to the horizontal position of the source projected on the caldera floor (409 m). The average slope of Okmok is a few degrees and well below the minimum threshold, 10°, suggested by *Cayol and Cornet* [1998], for which topographic effects become significant. The slope of the seafloor approaches 10° in a region about 10 km northwest of Umnak Island and within the simulated problem domain. However, the magnitude of deformation decays rapidly with distance from Okmok caldera (Figure 3d) and the effects of the slope of the seafloor are negligible. Deviation from the Poisson-solid assumption is easy to implement. Extensive tabulated values for Poisson's ratio for various rock types and confining pressures are readily available [*Christensen*, 1996]. These tables indicate that Poisson-solids are the exception, and not the rule. Neglecting an appropriate choice of Poisson's ratio can introduce significant, but unnecessary prediction errors that can be

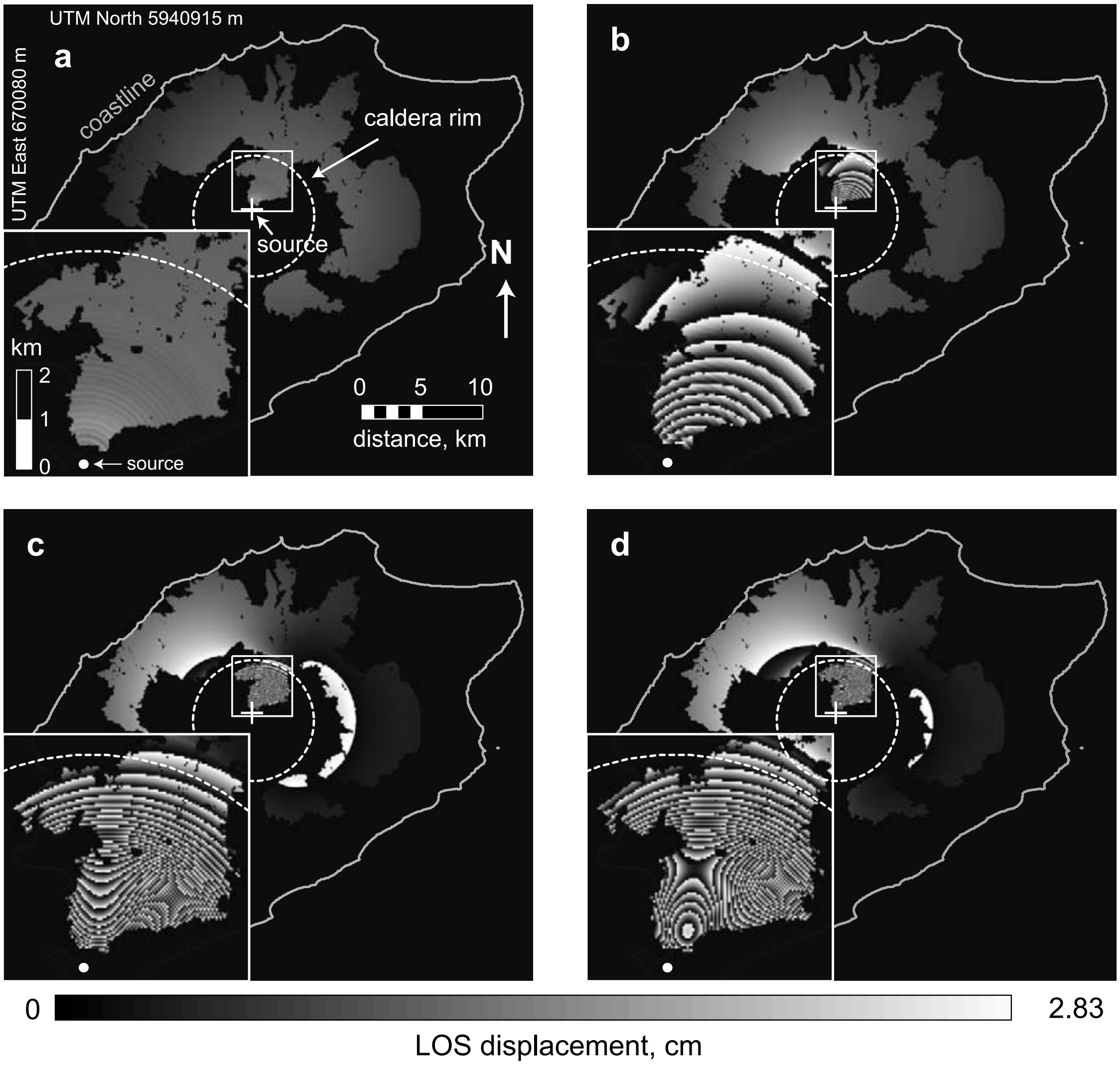

Figure 9. Forward model residuals: sensitivities to the homogeneous assumption. Each interferometric fringe, black-gray-white, represents 2.83 cm of deformation parallel to the LOS vector and toward the satellite. (a) $\mathbf{G}^{E}s^{A}$. (b) $\mathbf{G}^{F}s^{A}$. (c) $\mathbf{G}^{G}s^{A}$. (d) $\mathbf{G}^{H}s^{A}$. Sensitivity to regional-scale layering is negligible. Predicted deformation, from models simulating a weak caldera, severely overestimates that of the reference model.

eliminated by applying a linear correction (9) to *Mogi* [1958]. To the best of my knowledge, this study presents the first quantitative results that reveal the effects of elastic anisotropy on volcano deformation predictions. The anisotropy considered in this study substantially flattens the predicted deformation pattern. Previous analyses attributed flattening to either topographic effects [*Cayol and Cornet*, 1998] or the shape of the deformation source [e.g., *Dieterich and Decker*, 1975]. An observed "flattened" *Mogi* [1958] pattern of deformation may be the result of anisotropic elastic properties, topographic effects, a nonspherical source geometry, or most likely, some combination of these effects. Interpretations of observed flattening must consider all three of these effects.

[35] The volcano-wide deformation observed with the InSAR data captures a relatively local deformation field. Therefore the regional-scale heterogeneity of the simple layered system (Model E) did not significantly affect the predicted deformation pattern. This suggests that the additional complexity to account for regional-scale arc-parallel and arc-perpendicular heterogeneity of the subducting slab [*Fliedner and Klemperer*, 1999; *Lizarralde et al.*, 2002] is not necessary for volcano-wide deformation analyses. It is well known that systems of local-scale layering within a caldera profoundly affect local stress regimes and hence the propagation and arrest of dikes [e.g., *Gudmundsson and Philipp*, 2006]. A system of local layering is not tested in this analysis, although the anisotropic configuration of Model D can be viewed as a hypothetical configuration simulating the lower limit of layer thicknesses, for which the layering collapses to a transversely isotropic fabric.

[36] Local heterogeneity significantly impacts volcano deformation predictions. The relatively weak caldera structures simulated in this study act as strain conduits from a deformation source at the base of the caldera to the free surface of the caldera floor. Deformation predictions for the

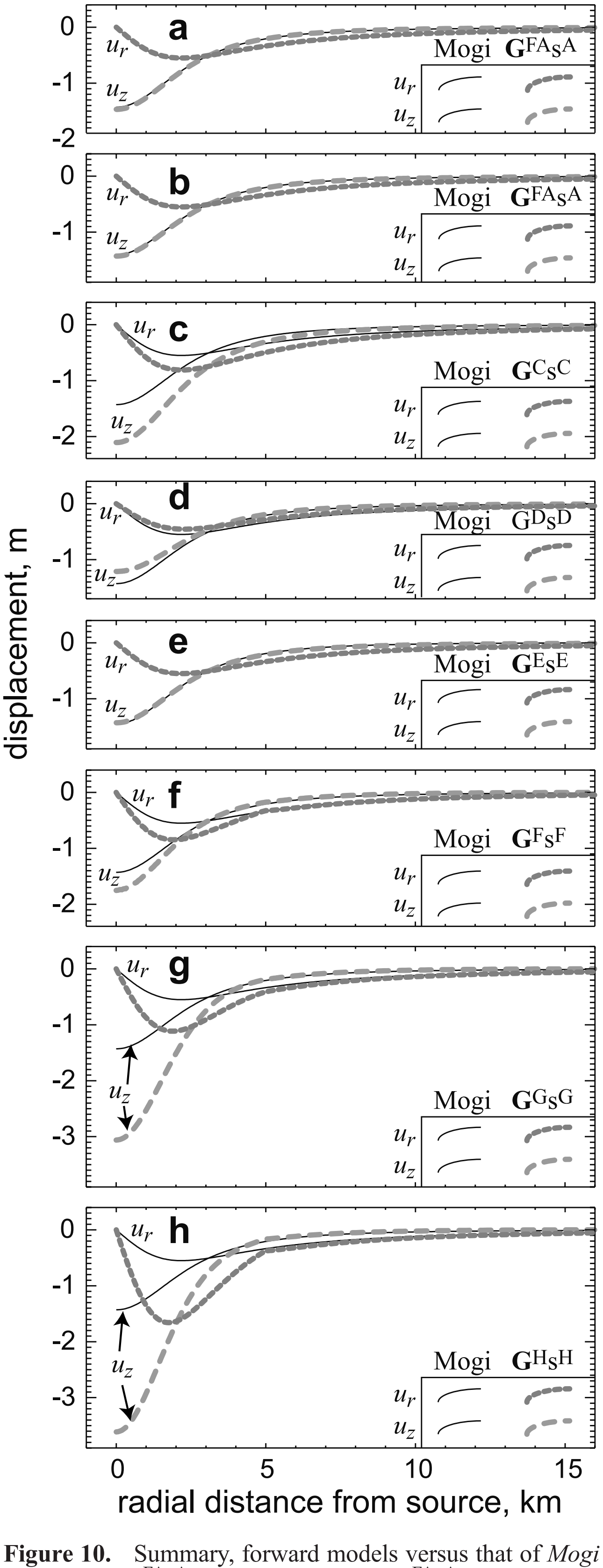

Figure 10. Summary, forward models versus that of *Mogi* [1958]. (a) $\mathbf{G}^{FA}s^{A}$, r_s = 1000 m. (b) $\mathbf{G}^{FA}s^{A}$, r_s = 500 m. (c) $\mathbf{G}^{C}s^{A}$. (d) $\mathbf{G}^{D}s^{A}$. (e) $\mathbf{G}^{E}s^{A}$. (f) $\mathbf{G}^{F}s^{A}$. (g) $\mathbf{G}^{G}s^{A}$. (h) $\mathbf{G}^{H}s^{A}$. This composite reveals the relative sensitivities to each of the HIPSHS assumptions, with respect to the work of *Mogi* [1958].

weak caldera configurations will produce a more "peaked" pattern of deformation for the caldera, with respect to the flanks of the volcano. The spatial resolution of the InSAR data provides relatively continuous sampling for the caldera floor and volcano flanks, as well as for the transition between these two regions. On the basis of the InSAR image (Figure 3), *Mann et al.* [2002] suggests the pattern of deformation is enhanced within the caldera and not consistent with a single *Mogi* [1958] source. Instead, deformation of the flanks is attributed to a *Mogi* [1958] source beneath the caldera and an additional shallow contracting "sill" [*Okada*, 1992] within the caldera accounts for the perceived excess subsidence of the caldera floor. The "sill" is interpreted as either real or a manifestation of the point-source geometry of *Mogi* [1958] deviating from the actual source geometry [*Mann et al.*, 2002]. If the HIPSHS assumptions are valid for Okmok volcano, then one of these interpretations of the "sill" is valid. If, however, the caldera material properties are different from those of the surrounding rock of the volcano, then a third possibility arises: the "sill" is merely an artifact of the HIPSHS model assumptions. Interpretations of volcano deformation that include a complex source geometry embedded in an HIPSHS problem domain, must also consider the possibility that the apparent source complexity may be a manifestation of a simple source geometry embedded in a complex non-HIPSHS problem domain.

[37] Comparisons of Figure 3c and Figure 12 indicate a particular residual pattern is an artifact of a particular deformation model. A previous InSAR-based analysis of posteruption deformation of Okmok volcano [*Lu et al.*, 2005a] interpreted the systematic residual from spherical expansion source models as deformation of lava flows that cover the caldera floor. The persistence of the residual in various posteruption InSAR images suggests that there is either significant mechanical complexity that is not accounted for by a spherical expansion source model or that there is indeed transient deformation of the caldera floor that is independent of the spherical expansion source. As demonstrated in this study, the interpretation of both cases is dependent on the model configuration chosen to simulate the deformational system.

[38] The magnitudes of the optimized expansion source pressures for the models considered in this study span 200–300 MPa (Figure 11). A similar result holds for pressures calculated using equation (2) and the estimated source volumes (ΔV) reported in previous studies InSAR-based studies of the 1997 eruption of Okmok volcano [*Lu et al.*, 1998, 2000a, 2005a; *Mann et al.*, 2002]. Lithostatic pressure is about 100 MPa for the estimated expansion source depths of the various models, which implies the problematic result that the pre-eruption pressure in the magma chamber was about three times greater than lithostatic conditions. Assuming a larger expansion source radius will reduce the estimated pressure of equation (2), although this configuration would clearly invalidate *Mogi*'s [1958] formulation owing to the shallow depths of the estimated expansion sources *McTigue* [1987]. Alternatively, modifying the FEMs to include a viscoelastic shell surrounding the expansion source will reproduce the net deformation over a finite time interval, while reducing the magnitude of the required source pressure [*Newman et al.*, 2001]. Transient

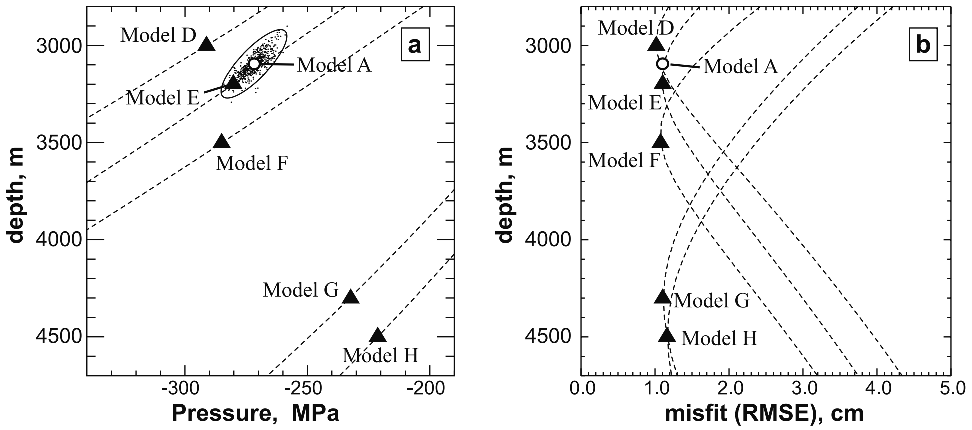

Figure 11. Inverse results for FEMs. (a) Spherical expansion source depth and pressure estimates. The 99% confidence ellipse and 500 realizations from Figure 4 are rescaled to fit the parameter space required for the FEM-based estimates. Dashed lines represent pressure estimates for suites of FEMs having perturbed spherical expansion source depths and reveal the coupled depth-pressure dependence. Results for Model FA are indistinguishable from those of Model A and the simple layered model (Model E) is not significantly different from the reference model (Model FA). (b) Misfit. The dashed lines show misfit results of sweeping through source depths of 2500–5000 m. The best fit RMSE misfit is about the same for all the models tested.

viscoelastic behavior is plausible during the two-year interval spanned by the image pair used to construct the InSAR data (Table 1) and the additional postseismic InSAR images [*Lu et al.*, 2005a] may provide viscosity constraints. However, this additional analysis is beyond the scope of this paper.

[39] The reliability of interpretations of volcano deformation, based on the results from a particular model, is a question of precision versus accuracy. Predictions from a model may precisely describe a given population of data. However, the accuracy of the predictions depends on how well the model represents the natural system in its entirety. For Okmok volcano, prediction sensitivities of both forward and inverse models are least sensitive to topographic effects and layered heterogeneity. Interestingly, these are often the only two deviations from the combined suite of HIPSHS assumptions considered in analyses of volcano deformation [e.g., *Cervelli et al.*, 2006; *Pritchard and Simons*, 2002]. Alternatively, both forward and inverse model predictions are most sensitive to lateral and local variations of material properties, for which prediction sensitivities far exceed expected deformation measurement uncertainties for GPS and InSAR observations. Source parameters estimated by inverting Model A (HIPSHS assumptions) and the InSAR data have uncertainties that are an order of magnitude smaller than the magnitudes of the estimated parameters (Figure 4). Other InSAR-based studies of deformation of Aleutian volcanoes, assessed with spherical expansion source models, also report similar relative parameter uncertainties [*Kwoun et al.*, 2006; *Lu et al.*, 1998, 2000a, 2000b, 2002a, 2002b, 2002c, 2003b, 2005a]. The accuracies of these precise estimates are subject to the validity of the models used to derive the parameter estimates. Nonetheless, the questions that emerge from the design, results, and interpretations of the models for Okmok volcano in this study require further reassessment.

5. Conclusions

[40] This study presents the first systematic examination, isolation, and assessment of each of the HIPSHS assumptions of *Mogi* [1958] and demonstrates the following: (1) a simple method for computing IRFs, using FEMs that do not require HIPSHS assumptions, for both forward and inverse models; (2) that displacement prediction errors, introduced by HIPSHS assumptions, can be severe; and (3) that deformation source parameters, precisely estimated from deformation data and standard inverse methods subject to HIPSHS assumptions, can be significantly inaccurate. The analysis of *Mogi* [1958] is suitable for qualitative assessments of volcano deformation. Quantitative assessments of volcano deformation require models that are more valid

Table 4. Spherical Expansion Source Parameters, Estimated From Inverse Models

Model	Impulse Response Function	Depth, m	P, MPa	RMSE, mm	Percentage of Reference Signal
FA	$\mathbf{G}^{FA}$	3100	−267	10.9	93.6
D	$\mathbf{G}^{D}$	3000	−291	10.1	94.1
E	$\mathbf{G}^{E}$	3200	−280	10.9	93.6
F	$\mathbf{G}^{F}$	3500	−285	10.8	93.5
G	$\mathbf{G}^{G}$	4300	−233	11.1	94.0
H	$\mathbf{G}^{H}$	4500	−221	11.7	93.7

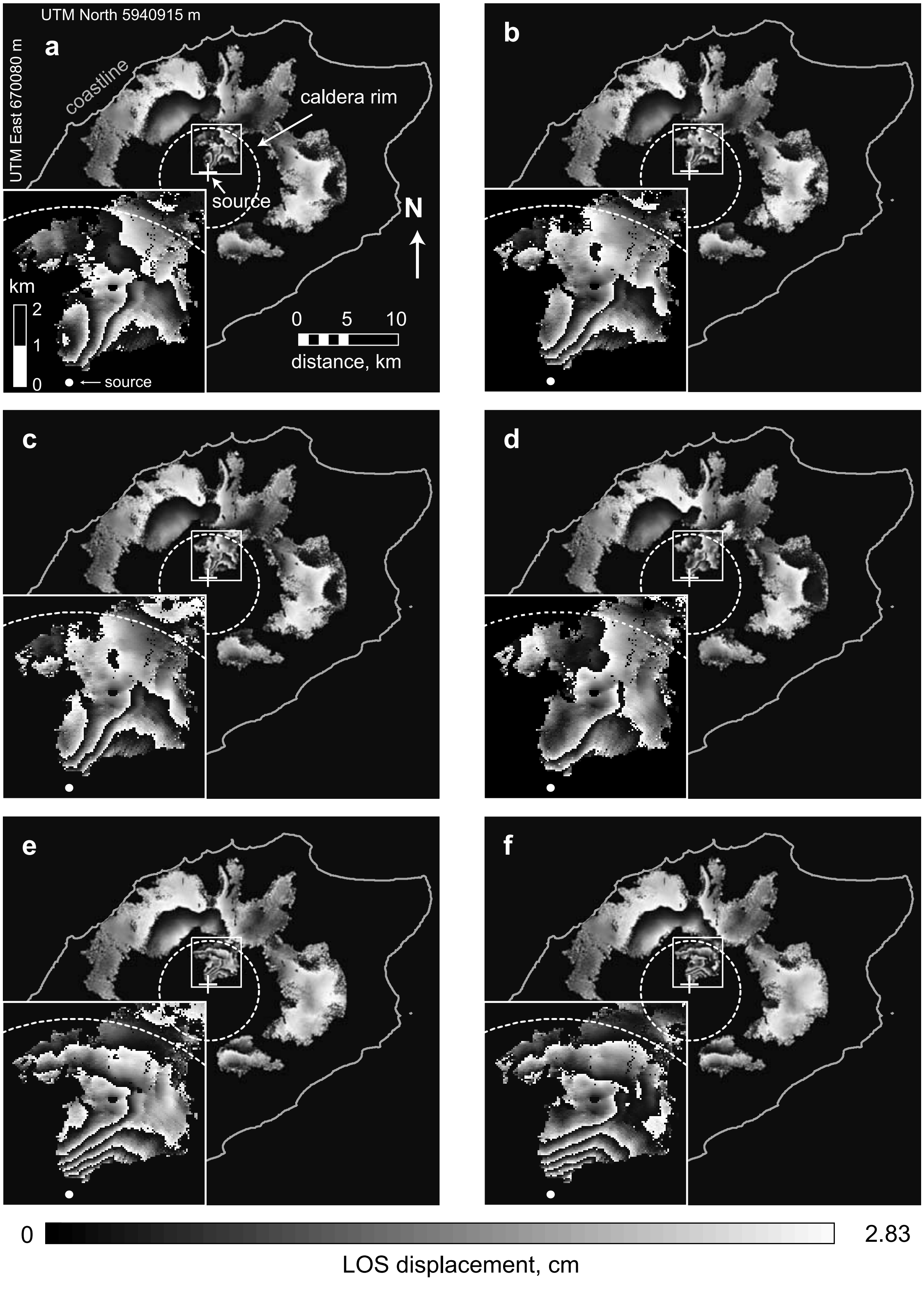

Figure 12. Residual images for FEM-generated impulse response functions (IRFs). Each image represents the difference between the observed data and the best fit predictions from the respective models. Each fringe, black-gray-white, represents 2.83 cm of deformation parallel to the LOS vector and toward the satellite. (a) $\mathbf{G}^{FA}s^{A}$, $r_s = 1000$ m. (b) $\mathbf{G}^{D}s^{D}$. (c) $\mathbf{G}^{E}s^{E}$. (d) $\mathbf{G}^{F}s^{F}$. (e) $\mathbf{G}^{G}s^{G}$. (f) $\mathbf{G}^{H}s^{H}$. The RMSE misfit is similar for all of these models, although there are systematic variations in the residual distribution that can be attributed to a given model configuration.

representations of natural volcano deformation systems. The results of this study are explicitly valid for the case of Okmok volcano and the observed deformation revealed in the associated InSAR data spanning the 1997 eruption. However, the general conclusions can be extended to other studies of volcano deformation.

[41] **Acknowledgments.** This research was supported in part by NASA NIP NNX06AF10G and the Tectonic Applications Project of the U.S. Geological Survey Land Remote Sensing Program. I thank ABAQUS Inc. for academic licensing and excellent technical support. Insightful reviews by P. Lundgren, G. Wadge, and Associate Editor T. Dixon greatly improved this paper.

References

Beauducel, F., G. De Natale, F. Obrizzo, and F. Pingue (2004), 3-D modeling of Campi Flegrei ground deformations: Role of caldera boundary discontinuities, *Pure Appl. Geophys.*, *161*, 1329–1344.

Bianchi, R., A. Coradini, C. Federico, G. Gilberti, P. Lanciano, J. P. Pozzi, F. Sartoris, and R. Scandone (1987), Modeling of surface ground deformation in volcanic areas: The 1970–1972 and 1982–1984 crises of Campi Flegrei, Italy, *J. Geophys. Res.*, *92*, 14,139–14,150.

Birch, F. (1960), The velocity of compressional waves in rocks to 10 kilobars: 1, *J. Geophys. Res.*, *65*, 1083–1102.

Bonaccorso, A., and P. M. Davis (1999), Models of ground deformation from vertical volcanic conduits with application to eruptions of Mount St. Helens and Mount Etna, *J. Geophys. Res.*, *104*, 10,531–10,542.

Bonaccorso, A., S. Cianetti, C. Giunchi, E. Trasatti, M. Bonafede, and E. Boschi (2005), Analytical and 3-D numerical modeling of Mt. Etna (Italy) volcano inflation, *Geophys. J. Int.*, *163*, 852–862.

Briole, P., D. Massonnet, and C. Delacourt (1997), Post-eruptive deformation associated with the 1986–87 and 1989 lava flows of Etna detected by radar interferometry, *Geophys. Res. Lett.*, *24*, 37–40.

Burgisser, A. (2005), Physical volcanology of the 2,050 BP caldera-forming eruption of Okmok volcano, Alaska, *Bull. Volcanol.*, *67*, 497–525, doi:10.1007/s00445-004-0391-5.

Cayol, V., and F. H. Cornet (1998), Effects of topography on the interpretation of the deformation field of prominent volcanoes: Application to Etna, *Geophys. Res. Lett.*, *25*, 1979–1982.

Cervelli, P., M. H. Murray, P. Segall, Y. Aoki, and T. Kato (2001), Estimating source parameters from deformation data, with an application to the March 1997 earthquake swarm off the Izu Peninsula, Japan, *J. Geophys. Res.*, *106*, 11,217–11,237.

Cervelli, P. F., T. Fournier, J. Freymueller, and J. A. Power (2006), Ground deformation associated with the precursory unrest and early phases of the January 2006 eruption of Augustine Volcano, Alaska, *Geophys. Res. Lett.*, *33*, L18304, doi:10.1029/2006GL027219.

Cheng, A. H.-D. (1997), Material coefficients of anisotropic poroelasticity, *Int. J. Rock Mech. Min. Sci.*, *34*, 199–205.

Christensen, N. I. (1996), Poisson's ratio and crustal seismology, *J. Geophys. Res.*, *101*, 3139–3156.

Christensen, N. I., and W. Mooney (1995), Seismic velocity structure and composition of the continental crust: A global view, *J. Geophys. Res.*, *100*, 9761–9788.

Davis, J. C. (2002), *Statistics and Data Analysis in Geology*, 639 pp., John Wiley, New York.

De Natale, G., and F. Pingue (1996), Ground deformation modeling of volcanic areas, in *Monitoring and Mitigation of Volcanic Hazards*, edited by R. Scarpa and R. I. Tilling, pp. 365–388, Springer-Verlag, Berlin.

De Natale, G., S. M. Petrazzuoli, and F. Pingue (1997), The effect of collapse structures on ground deformations in calderas, *Geophys. Res. Lett.*, *24*, 1555–1558.

Dieterich, J. H., and R. W. Decker (1975), Finite element modeling of surface deformation associated with volcanism, *J. Geophys. Res.*, *80*, 4094–4102.

Dragoni, M., and C. Magnanensi (1989), Displacement and stress produced by a pressurized, spherical magma chamber, surrounded by a viscoelastic shell, *Phys. Earth Planet. Inter.*, *56*, 316–328.

Dvorak, J. J., and D. Dzurisin (1997), Volcano geodesy: The search for magma reservoirs and the formation of eruptive vents, *Rev. Geophys.*, *35*, 343–384.

Dzurisin, D. (2003), A comprehensive approach to monitoring volcano deformation as a window on the eruption cycle, *Rev. Geophys.*, *41*(1), 1001, doi:10.1029/2001RG000107.

Fernández, J., J. B. Rundle, R. D. R. Granell, and T.-T. Yu (1997), Programs to compute deformation doe to a magma intrusion in elastic-gravitational layered Earth models, *Comput. Geosci.*, *23*, 231–249.

Fialko, Y., M. Simons, and Y. Khazan (2001), Finite source modeling of magmatic unrest in Socorro, New Mexico, and Long Valley, California, *Geophys. J. Int.*, *146*, 191–200.

Fliedner, M. M., and S. L. Klemperer (1999), Structure of an island-arc: Wide angle seismic studies in the eastern Aleutian Islands, Alaska, *J. Geophys. Res.*, *104*, 10,667–10,694.

Godfrey, N. J., N. I. Christensen, and D. A. Okaya (2000), Anisotropy of schists: Contribution of anisotropy to active source seismic experiments and shear-wave splitting, *J. Geophys. Res.*, *105*, 27,991–28,007.

Gottsmann, J., A. Folch, and H. Rymer (2006a), Unrest and Campi Flegrei: A contribution to the magmatic versus hydrothermal debate from inverse and finite element modeling, *J. Geophys. Res.*, *111*, B07203, doi:10.1029/2005JB003745.

Gottsmann, J., H. Rymer, and G. Berrino (2006b), Unrest at Campi Flegrei: A critical evaluation of source parameters from geodetic data inversion, *J. Volcanol. Geotherm. Res.*, *150*, 132–145.

Gudmundsson, A., and I. F. Loetveit (2005), Dyke emplacement in a layered and faulted rift zone, *J. Volcanol. Geotherm. Res.*, *144*, 311–327.

Gudmundsson, A., and S. Philipp (2006), How local stress fields prevent volcanic eruptions, *J. Volcanol. Geotherm. Res.*, *158*, 257–268.

Kwoun, O.-I., Z. Lu, C. Neal, and C. Wicks Jr. (2006), Quiescent deformation of the Aniakchak Caldera, Alaska, mapped by InSAR, *Geology*, *34*, 5–8.

Lizarralde, D., W. S. Holbrook, S. McGeary, N. L. Bangs, and J. B. Diebold (2002), Crustal construction of a volcanic arc, wide-angle seismic results from the western Alaska Peninsula, *J. Geophys. Res.*, *107*(B8), 2164, doi:10.1029/2001JB000230.

Lu, Z., and J. T. Freymueller (1998), Synthetic aperture radar interferometry coherence analysis over Katmai volcano group, Alaska, *J. Geophys. Res.*, *103*, 29,887–29,894.

Lu, Z., D. Mann, and J. T. Freymueller (1998), Satellite radar interferometry measures deformation of Okmok volcano, *Eos Trans. AGU*, *79*(39), 461, 467–468.

Lu, Z., D. Mann, J. T. Freymueller, and D. J. Meyer (2000a), Synthetic aperture interferometry of Okmok volcano, Alaska: Radar observations, *J. Geophys. Res.*, *105*, 10,791–10,806.

Lu, Z., C. W. Wicks Jr., J. A. Power, and D. Dzurisin (2000b), Ground deformation associated with the March 1996 earthquake swarm at Akutan volcano, Alaska, revealed by satellite radar interferometry, *J. Geophys. Res.*, *105*, 21,483–21,495.

Lu, Z., C. Wicks, D. Dzurisin, W. Thatcher, J. T. Freymueller, S. R. McNutt, and D. Mann (2000c), Aseismic inflation of Westdahl volcano, Alaska, revealed by satellite radar interferometry, *Geophys. Res. Lett.*, *27*, 1567–1570.

Lu, Z., C. W. Wicks Jr., D. Dzurisin, J. A. Power, S. C. Moran, and W. Thatcher (2002a), Magmatic inflation at a dormant stratovolcano: 1996–1998 activity at Mount Peulik volcano, Alaska, revealed by satellite radar interferometry, *J. Geophys. Res.*, *107*(B7), 2134, doi:10.1029/2001JB000471.

Lu, Z., J. A. Power, V. S. McConnell, C. W. Wicks Jr., and D. Dzurisin (2002b), Preeruptive inflation and surface interferometric coherence characteristics revealed by satellite radar interferometry at Makushin volcano, Alaska: 1993–2000, *J. Geophys. Res.*, *107*(B11), 2266, doi:10.1029/2001JB000970.

Lu, Z., T. Masterlark, J. Power, D. Dzurisin, C. Wicks Jr., and W. Thatcher (2002c), Subsidence at Kiska volcano, western Aleutians, detected by satellite radar interferometry, *Geophys. Res. Lett.*, *29*(3), 1855, doi:10.1029/2002GL014948.

Lu, Z., C. Wicks Jr., D. Dzurisin, J. Power, W. Thatcher, and T. Masterlark (2003a), Interferometric synthetic aperture radar studies of Alaska volcanoes, *Earth Obs. Mag.*, *12*(3), 8–18.

Lu, Z., T. Masterlark, D. Dzurisin, R. Rykhus, and C. Wicks Jr. (2003b), Magma supply dynamics at Westdahl volcano, Alaska, modeled from satellite radar interferometry, *J. Geophys. Res.*, *108*(B7), 2354, doi:10.1029/2002JB002311.

Lu, Z., T. Masterlark, and D. Dzurisin (2005a), Interferometric synthetic aperture study of Okmok volcano, Alaska: Magma supply dynamics and post-emplacement lava flow deformation, *J. Geophys. Res.*, *110*, B02403, doi:10.1029/2004JB003148.

Lu, Z., C. Wicks Jr., O. Kwoun, J. A. Power, and D. Dzurisin (2005b), Surface deformation associated with the March 1996 earthquake swarm at Akutan Island, Alaska, revealed by C-band ERS and L-band JERS radar interferometry, *Can. J. Remote Sens.*, *31*(1), 7–20.

Lundgren, P., P. Berardino, M. Coltelli, G. Fornaro, R. Lanari, G. Puglisi, E. Sansosti, and M. Tesauro (2003), Coupled magma chamber inflation and sector collapse slip observed with synthetic aperture radar interferometry on Mt. Etna volcano, *J. Geophys. Res.*, *108*(B5), 2247, doi:10.1029/2001JB000657.

Mann, D., J. Freymueller, and Z. Lu (2002), Deformation associated with the 1997 eruption of Okmok volcano, Alaska, *J. Geophys. Res.*, *107*(B4), 2072, doi:10.1029/2001JB000163.

Massonnet, D., and K. Feigl (1998), Radar interferometry and its application to changes in the Earth's surface, *Rev. Geophys.*, *36*, 441–500.

Masterlark, T. (2003), Finite element model predictions of static deformation from dislocation sources in a subduction zone: Sensitivities to homogeneous, isotropic, Poisson-solid, and half-space assumptions, *J. Geophys. Res.*, *108*(B11), 2540, doi:10.1029/2002JB002296.

Masterlark, T., and Z. Lu (2004), Transient volcano deformation sources imaged with interferometric synthetic aperture radar: Application to Seguam Island, Alaska, *J. Geophys. Res.*, *109*, B01401, doi:10.1029/2003JB002568.

Masterlark, T., Z. Lu, and R. Rykhus (2006), Thickness distribution of a cooling pyroclastic flow deposit: Optimization using InSAR, FEMs, and an adaptive mesh algorithm, *J. Volcanol. Geotherm. Res.*, *150*, 186–201.

McTigue, D. F. (1987), Elastic stress and deformation near a finite spherical magma body: Resolution of the point source paradox, *J. Geophys. Res.*, *92*, 12,931–12,940.

Miller, A. D., B. R. Julian, and G. R. Foulger (1998a), Three-dimensional seismic structure and moment tensors of non-double-couple earthquakes at the Hengill-Grensdalur volcanic complex, Iceland, *Geophys. J. Int.*, *133*, 309–325.

Miller, T. P., R. G. McGimsey, D. H. Richter, J. R. Riehle, C. J. Nye, M. E. Yount, and J. A. Dumoulin (1998b), Catalog of the historically active volcanoes of Alaska, *U.S. Geol. Surv. Open File Rep.*, *98-582*, 104 pp.

Miyagi, Y., J. T. Freymueller, F. Kimata, T. Sato, and D. Mann (2004), Surface deformation caused by shallow magmatic activity at Okmok volcano, Alaska, detected by GPS campaigns 2000–2002, *Earth Planet. Space*, *56*, e29–e32.

Mogi, K. (1958), Relations between the eruptions of various volcanoes and the deformations of the ground surface around them, *Bull. Earthquake Res. Inst. Univ. Tokyo*, *36*, 99–134.

Moran, S. C., O. Kwoun, T. Masterlark, and Z. Lu (2006), On the absence of InSAR-detected volcano deformation spanning the 1995–1996 and 1999 eruptions of Shishaldin Volcano, Alaska, *J. Volcanol. Geotherm. Res.*, *150*, 119–131.

Newman, A. V., T. H. Dixon, G. I. Ofoegbu, and J. E. Dixon (2001), Geodetic and seismic constraints on recent activity at Long Valley Caldera, California: Evidence for viscoelastic rheology, *J. Volcanol. Geotherm. Res.*, *105*, 183–206.

Newman, A. V., T. H. Dixon, and N. Gourmelen (2006), A four-dimensional viscoelastic model for Long Valley Caldera, California, between 1995 and 2000, *J. Volcanol. Geotherm. Res.*, *150*, 244–269.

Nur, A., and J. Walder (1992), Hydraulic pulses in the Earth's crust, in *Fault Mechanics and Transport Properties of Rocks*, edited by B. Evans and T. F. Wong, pp. 461–473, Academic, London.

Okada, Y. (1992), Internal deformation due to shear and tensile faults in a half-space, *Bull. Seismol. Soc. Am.*, *82*, 1018–1040.

Orsi, G., S. M. Petrazzuoli, and K. Wohletz (1999), Mechanical and thermo-fluid behavior during unrest at the Campi Flegrei caldera (Italy), *J. Volcanol. Geotherm. Res.*, *91*, 453–470.

Patrick, M. R., J. Dehn, and K. Dean (2004), Numerical modeling of lava flow cooling applied to the 1997 Okmok eruption: Approach and analysis, *J. Geophys. Res.*, *109*, B03202, doi:10.1029/2003JB002537.

Poland, M., R. Bürgmann, D. Dzurisin, M. Lisowski, T. Masterlark, S. Owen, and J. Fink (2006), Constraints on the mechanism of long-term, steady subsidence at Medicine Lake volcano, northern California, from GPS and precise leveling, *J. Volcanol. Geotherm. Res.*, *150*, 55–78.

Press, W., S. Teukolsky, W. Vetterling, and B. Flannery (1992), *Numerical Recipes in C: The Art of Scientific Computing*, 994 pp., Cambridge Univ. Press, New York, 1992.

Price, E. J. (2004), Dynamic deformation of Seguam Island, Aleutian Islands, Alaska, 1993–2000: Implications for magmatic and hydrothermal processes, *J. Geophys. Res.*, *109*, B04202, doi:10.1029/2003JB002671.

Pritchard, M. E., and M. Simons (2002), A satellite geodetic survey of large-scale deformation on volcanic centres in the central Andes, *Nature*, *418*, 167–171.

Rundle, J. B. (1980), Static elastic-gravitational deformation of a layered half space by point couple sources, *J. Geophys. Res.*, *85*, 5355–5363.

Singer, B. S., J. D. Meyers, and C. D. Frost (1992), Mid-Pleistocene basalt from the Seguam volcanic center, central Aleutian arc, Alaska: Local lithospheric structures and source variability in the Aleutian arc, *J. Geophys. Res.*, *97*, 4561–4578.

Stern, R. J. (2002), Subduction zones, *Rev. Geophys.*, *40*(4), 1012, doi:10.1029/2001RG000108.

Stevens, N. F., G. Wadge, C. A. Williams, J. G. Morley, J.-P. Muller, J. B. Murray, and M. Upton (2001), Surface movements of emplaced lava flows measured by synthetic aperture radar interferometry, *J. Geophys. Res.*, *106*, 11,293–11,313.

Sturkell, E., P. Einarsson, F. Sigmundsson, H. Geirsson, H. Ólafsson, R. Pedersen, E. de Zeeuw-van Dalfsen, A. T. Linde, S. I. Sacks, and R. Stefánsson (2006), Volcano geodesy and magma dynamics in Iceland, *J. Volcanol. Geotherm. Res.*, *150*, 14–34.

Trasatti, E., C. Giunchi, and M. Bonafede (2003), Effects of topography and rheological layering on ground deformation in volcanic regions, *J. Volcanol. Geotherm. Res.*, *122*, 89–110.

Trasatti, E., C. Giunchi, and M. Bonafede (2005), Structural and rheological constraints on source depth and overpressure estimates at the Campi Flegrei caldera, Italy, *J. Volcanol. Geotherm. Res.*, *144*, 105–118.

Troise, C., F. Pingue, and G. De Natale (2003), Coulomb stress changes at calderas: Modeling the seismicity of Campi Flegrei (southern Italy), *J. Geophys. Res.*, *108*(B6), 2292, doi:10.1029/2002JB002006.

Turcotte, D. L., and G. J. Schubert (1982), *Geodynamics: Applications of Continuum Physics to Geological Problems*, 450 pp., John Wiley, New York.

Vogfjörd, K. S., et al. (2005), Forecasting and monitoring a subglacial eruption in Iceland, *Eos Trans. AGU*, *86*(26), 248.

Wang, H. F. (2000), *Theory of Linear Poroelasticity: With Applications to Geomechanics*, 287 pp., Princeton Univ. Press, Princeton, N. J.

Wang, H. F., and M. P. Anderson (1982), *Introduction to Groundwater Modeling: Finite Difference and Finite Element Methods*, 237 pp., Academic, San Diego, Calif.

Wicks, C. W., Jr., D. Dzurisin, S. Ingebristen, W. Thatcher, Z. Lu, and J. Iverson (2002), Magmatic activity beneath the quiescent Three Sisters volcanic center, central Oregon Cascade Range, USA, *Geophys. Res. Lett.*, *29*(7), 1122, doi:10.1029/2001GL014205.

Williams, C. A., and G. Wadge (1998), The effects of topography on magma chamber deformation models: Application to Mt. Etna and radar interferometry, *Geophys. Res. Lett.*, *25*, 1549–1552.

Williams, C. A., and G. Wadge (2000), An accurate and efficient method for including the effects of topography in three-dimensional elastic models of ground deformation with applications to radar interferometry, *J. Geophys. Res.*, *105*, 8103–8120.

Yang, X. M., P. M. Davis, and J. H. Dieterich (1988), Deformation from inflation of a dipping finite prolate spheroid in an elastic half-space as a model for volcanic stressing, *J. Geophys. Res.*, *93*, 4249–4257.

Yun, S., P. Segall, and H. Zebker (2006), Constraints on magma chamber geometry at Sierra Negra Volcano, Galápagos Islands, based on InSAR observations, *J. Volcanol. Geotherm. Res.*, *150*, 232–243.

Zoback, M. L. (1992), First- and second-order patterns of stress in the lithosphere: The world stress map project, *J. Geophys. Res.*, *97*, 11,703–11,728.

T. Masterlark, Department of Geological Sciences, University of Alabama, Tuscaloosa, AL 35487, USA. (masterlark@geo.ua.edu)